Thermodynamic study and the development of a support vector machine model for predicting adsorption behavior of orange peel-derived beads in wastewater treatment

Abderraouf Guediri, Abdallah Bouguettoucha, Hichem Tahraoui, Derradji Chebli, Abdeltif Amrane, Jie Zhang

Thermodynamic Study and the Development of a Support Vector Machine Model for Predicting Adsorption Behavior of Orange Peel-Derived Beads in Wastewater Treatment

Abderraouf Guediri[a,a.guediri@univ-setif.dz], Abdallah Bouguettoucha[a,abdallah.bouguettoucha@univ-setif.dz], Hichem Tahraoui[a,b,*,hichemm.tahraouii@gmail.com,hichem.tahraoui@ univ-setif.dz], Derradji Chebli[a,derradji_chebli@yahoo.fr], Abdeltif Amrane[b,abdeltif.amrane@univ-rennes1.fr], Jie Zhang[c,jie.zhang@newcastle.ac.uk]

[a]Département de Génie des Procédés, Laboratoire de Génie des Procédés Chimiques, Faculté de Technologie, Université Ferhat Abbas, Sétif-1, 19000 Sétif, Algérie

[b]Univ Rennes, Ecole Nationale Supérieure de Chimie de Rennes, CNRS, ISCR – UMR6226, F-35000 Rennes, France

[c]School of Engineering, Merz Court, Newcastle University, Newcastle upon Tyne NE1 7RU, UK

[*]**Corresponding author.**

Abstract

This study investigates the use of orange peels as a precursor for synthesizing sodium alginate-encapsulated beads for methylene blue (MB) removal. The prepared beads (BOP1 and BOP2) underwent characterization through FTIR, XRF, SEM and TGA. Subsequently, the impacts of various factors, including temperature, the initial pH, initial concentration, salt and humic acid, are studied. The adsorption isotherms show high adsorbed quantities of 764.92 and 659.78 mg/g for BOP1 and BOP2 respectively, while the obtained data are best described by the monolayer

with two energies (MMTE) model, which is then used to perform a thermodynamic study of the MB adsorption mechanism. Additionally, the adsorption kinetics data are modeled using three models, with the PFO model identified as the most appropriate. The regenerated beads demonstrate the ability to be reused up to 7 cycles, The effects of NaCl and humic acid on MB adsorption reveal that NaCl inhibits adsorption due to competition with Na+, while humic acid has no effect. Finally, a support vector machine (SVM) model optimized by the Levy Flight Distribution Optimization (LFD) algorithm is developed and found to be capable of accurately predicting the adsorption behavior of the prepared beads. This model is then used in optimizing the process conditions for maximal MB removal. Overall, this study demonstrates that the prepared beads could be potential low-cost and environmentally friendly adsorbents for wastewater treatment applications.

Graphical Abstract

Keywords: Adsorption, orange peel beads, methylene blue, support vector machine, Levy flight distribution, thermodynamic

1. Introduction

The textile, pharmaceutical, paper, cosmetics, and plastics industries generate substantial effluent, containing a diverse range of substances [1]. Even at low concentrations, these

substances can pose risks to both human health and the environment, especially when they are not biodegradable [2]. Moreover, it is estimated that more than 10,000 tons of dye and coloring agents are used each year, resulting in the release of 40,000 tons of dye into the environment each year [3]. In this context, various methods such as membrane filtration [4], oxidation [5], coagulation [6], photocatalysis [7], and other biological processes have been employed to treat these effluents. However, these techniques show some drawbacks such as weak performance, high cost and high secondary pollution [8]. As a consequence, adsorption is still the most used method due to its simplicity, effectiveness, and low cost [9].

Even though adsorption is an effective process for reducing contamination in discharges, its optimization is challenging due to its nonlinear and complex nature [10]. The conventional method of optimizing parameters by varying one independent variable while keeping the others constant is tedious and requires numerous time consuming experiments [10]. Additionally, accurately optimizing the interaction effect of multiple independent variables and analyzing the relationship between a large number of independent and dependent variables becomes difficult [11]. To address this challenge, researchers have started utilizing artificial intelligence techniques such as: intelligent modeling and experimental study on methylene blue adsorption by sodium alginate-kaolin beads [12]; application of machine/statistical learning, artificial intelligence and statistical experimental design for the modeling and optimization of methylene blue and Cd (ii) removal from a binary aqueous solution by natural walnut carbon [13]; and decontamination of methylene blue from simulated wastewater by the mesoporous rGO/Fe/Co nanohybrids through artificial intelligence modeling and optimization [14].

In this study, the synthetic cationic methylene blue (MB) dye is chosen as the test molecule due to its wide range of applications, stability, high solubility (40g/L), and non-biodegradability at concentrations exceeding 5 mg/L [15]. Furthermore, it poses a potential hazard in the event of accumulation in human and animal organs [16], leading to a reduction in water oxygen

concentration and adverse effects on the photosynthetic activity of plants [15,17]. According to the literature, a variety of products have been used as adsorbents, including activated carbon [18], zeolites [19], clays [20], silica [21], agricultural waste [22], and hydrogels [23] , each with its own advantages and disadvantages. In this article, the preparation of adsorbent materials was performed using waste orange peels as a precursor. The peels underwent chemical treatment with phosphoric acid and were subsequently encapsulated in different ratios using sodium alginate.

It is important to highlight that encapsulation served diverse purposes, including the attainment of a durable material with a uniform shape, enhancement of adsorption efficiency, provision of a material separable from the solution and thermally stable, thus aligning with industrial applications, and finally facilitating the regeneration step [24]. In addition, alginate was used as an encapsulating agent due to the negative charge of its carboxyl groups [25], which promotes the adsorption of cationic compounds. The prepared materials were characterized using several techniques, including FTIR, XRF, SEM, TGA, and the isoelectric point. Adsorption kinetics were analyzed and fitted using the pseudo-first-order (PFO), pseudo-second-order (PSO), pseudo-nth-order (PNO), intraparticle, and Boyd models. Furthermore, in consideration of their simplicity and applicability [2], the two classical models of Langmuir and Freundlich were employed to analyze the obtained results from MB adsorption isotherms in order to obtain interpretations for the interaction mechanism nature between MB and the prepared beads; moreover, these last two models were unsatisfactory for the intended purpose, as they failed to provide physicochemical interpretations of the adsorption mechanism [26,27]. As a consequence of these findings, the grand canonical partition function in statistical physics was employed to offer more detailed and precise insights into the adsorption process [28], which can be seen from the information derived from parameters obtained through statistical models, including the density of the receptor sites (Ns), the number of molecules captured by

the adsorbent receptor site (n_{im}), the half-saturation concentration, adsorption energy, and adsorbed amount at saturation (Q_{sat}), etc. Following this approach, three statistical physical models namely, monolayer with single energy (MMSE), monolayer with two energies (MMTE), and double layer with two energies (DMTE), were considered to elucidate the experimental results of MB adsorption isotherms on the beads prepared at various temperatures (10, 25 and 30 °C).

Moreover, the most accurate statistical physic model parameters were used to calculate, plot and assess the variation of internal energy, Gibbs free enthalpy, and configuration entropy to perform a thermodynamic study for MB adsorption mechanism on the prepared beads (BOP1 and BOP2). At the end, the Levy Flight Distribution (LFD) optimization algorithm was used to improve the SVM model to predict the amount of MB adsorption on BOP1 and BOP2 using the experimental results of adsorption parameter optimization. Further optimization was performed using LFD and the SVM-LFD model to obtain optimal process conditions for maximal MB removal. Additionally, a MATLAB-based user-friendly tool was created to simplify the process of MB adsorption optimization and prediction.

This study introduces significant innovations by integrating novel materials and advanced methodologies into the realm of MB adsorption. Departing from conventional choices, orange peels were utilized as a unique precursor for synthesizing beads dedicated to MB removal, offering a distinctive perspective in the field. Through a dual modification process involving treatment with H_3PO_4 and encapsulation with sodium alginate, a substantial improvement in the adsorption capacity of these beads was achieved.

Beyond the experimental findings, the investigation provides a comprehensive understanding of the adsorption mechanism and thermodynamic behavior, employing three physical models—MMSE, MMTE, and DMTE—with the MMTE model identified as the most suitable. Furthermore, this study introduces an innovative computational paradigm represented by the

SVM-LFD approach for predicting and optimizing MB adsorption capacity, thus adding a novel dimension to the research landscape. Importantly, such a study has not been undertaken previously, marking it as a pioneering endeavor.

To enhance the accessibility of the findings, a user-friendly MATLAB-based tool for MB adsorption optimization and prediction was developed. Collectively, these innovative elements distinguish the work and signify a noteworthy progression in the field of MB adsorption research.

2. Materials and methods

2.1. Materials

All chemicals employed in this research, including methylene blue (MB), H_3PO_4, HCl, NaOH, $CaCl_2$, NaCl, humic acid (HA), and sodium alginate (SA), were obtained from Sigma Aldrich. Orange peels were collected after the fruit had been consumed.

2.2. Products preparation

The procedure for treating orange peels with phosphoric acid was the same as described in our published paper [29], and the resulting powder was named as treated orange peels (TOP). To immobilize TOP, 1g of it was mixed with 1 g of SA in 100 ml of distilled water for BOP1, while the TOP/SA ratio was set to 2 for BOP2. The mixture was then stirred until homogenization. Encapsulation was performed by adding the mixture dropwise into a 40% $CaCl_2$ solution using a peristaltic pump and vigorous stirring to avoid rapid depletion of Ca^{2+} ions. The resulting beads, named BOP1 and BOP2, were stirred for 12 hours to ensure the creation of an "egg box"[30]. The beads were then washed seven times with distilled water and dried at room temperature.

2.3. Adsorption kinetics

Adsorption kinetics is a key step in determining the rate at which equilibrium is reached and can aid in understanding the adsorption mechanisms and developing a fast and effective adsorption model [31–34]. In this study, batch adsorption tests were performed at natural dye pH (6.2) to evaluate the amount of adsorption as a function of time using three initial concentrations of methylene blue (MB) (50, 100, and 200 mg/L). 200 mg of adsorbent were put into contact with 200 mL of each initial concentration of MB at room temperature (25 °C ± 2 °C). The amount of adsorption was regularly measured until equilibrium was reached, ensuring that the total volume of samples did not exceed 10% of the initial solution. The samples were analyzed using a Shimadzu Spectrophotometer UV-1700, and the amount of adsorption was determined using Eq. 1:

$$Q_{ads} = \frac{V*(C_0 - C_t)}{m} (1)$$

Moreover, the MB adsorption on the prepared beads was analyzed using various kinetic models, including the pseudo-first order (PFO), pseudo-second order (PSO), pseudo-nth order (PNO), intraparticle, and Boyd models, as given by Eqs. S1 to S5 (a,b) [35–39].

2.4. Adsorption isotherms

50 mg of each material was mixed with 50 ml of MB dye at natural pH (6.2), with initial concentrations ranging from 50 to 1200 mg/L, and the mixtures were left in contact with constant stirring around 250 rpm at well-controlled temperatures (10, 25, and 30 °C, 2 ± °C) until equilibrium being achieved. Then, each solution was separated and analyzed by UV visible. Moreover, classical models, including the most commonly reported models in the literature, Langmuir and Freundlich [40], and other statistical physics models have been employed to understand MB adsorption mechanism on BOP. It is well known that Langmuir's model is based on three main assumptions: first, adsorption occurs in a single layer, second, the distribution of active sites is uniform, and third, adsorption energies are independent. On the

other hand, the Freundlich model assumes that the adsorption is heterogeneous and occurs in multilayer [41].

Eqs. S6 and S7 present the mathematical expressions for the Langmuir and Freundlich models, respectively [42–44].

2.5. Statistical physical modeling

To provide more profound and precise interpretations for the MB adsorption mechanism on BOP [28], physical modeling was considered using statistical physics models based on applying the grand canonical partition function in statistical physics. The three models applied are detailed in the following subsection.

2.5.1. Monolayer model with single energy: MMSE

This model assumes that the adsorption occurs in a monolayer with only one energy [45]. The demonstration of the applied physical models needs to go through the use of the grand canonical partition function in statistical physics. The grand canonical partition function of one site is given as follows in Eq. 2 [46] :

$$z_{gc} = 1 + e^{\beta(\varepsilon_1+\mu)} \quad (2)$$

Then, Eq. 3 presents the grand canonical partition function relative to the density of receptor sites, which is assumed to be identical and independent [47].

$$Z_{gc}(Ns) = (z_{gc})^{Ns} \quad (3)$$

As a result, it is possible to write that [46]:

$$Z_{gc}(Ns) = (1 + e^{\beta(\varepsilon_1+\mu)})^{Ns} \quad \text{.....4}$$

As a consequence, the average site occupation number is given according to Eq. 5 [48] :

$$N_0 = \frac{N_s \partial ln z_{gc}}{\beta \partial \mu} \quad \text{.....5}$$

Furthermore, in an adsorption process of a binary system (for example, the adsorption of MB on BOP in this study), it is possible to write that:

$n_m MB + BOP \leftrightarrow MB_{nm}BOP$……..…….6

At thermodynamic equilibrium, Eq. 6 provides the relationship between the chemical potentials of dissolved molecules μ_m and that of adsorbed molecules μ as a function of the translational partition function, as seen in Eq. 7 [26] :

$$\mu_m = \frac{\mu}{n_m} = k_B T ln(Ns/Z_{gtr}) \quad \text{.....7}$$

Eq. 8 can be used to express the translation partition function [49]:

$$z_{gtr} = V\left(\frac{2\pi m}{\beta h^2}\right)^{3/2} \quad \text{.....8}$$

Furthermore, the adsorbed quantity at saturation is given by Eq. 9 [47]:

$$Q_{sat} = n_{im} N_{iS} \quad \text{.....9}$$

Taking all previous equations into consideration, the monolayer model with single energy (MMSE) is given by Eq. 10 [50]:

$$Q_{ads} = \frac{n_m N_S}{\left(1 + \left(\frac{C_{1/2}}{C_e}\right)^{n_m}\right)} \quad \text{.....10}$$

Furthermore, the quantity adsorbed at saturation for this model is established by Eq. 11:

$$Q_{sat} = n_m N_S \quad \text{.....11}$$

It is worth noting that MMSE can provide a number of adsorbates equal to or greater than unity on a single adsorption site [51].

2.5.2. Monolayer model with two energies: MMTE

For this model, the derivation procedure is the same as that carried out for the MMSE, except that its grand canonical partition functions are given according to Eqs. 12 and 13 [52], while one related to the receptor sites is by given Eq. 14 [53]:

$$z_{1gc} = 1 + e^{\beta(\varepsilon_1+\mu_1)} \quad \text{.....12}$$

$$z_{2gc} = 1 + e^{\beta(\varepsilon_2+\mu_2)} \quad \text{.....13}$$

Where, z_{1gc} and z_{2gc} represent the partition functions corresponding to the two types of sites.

$$Z_{gc}(N_S) = (1 + e^{\beta(\varepsilon_1+\mu_1)})^{N_{1S}}(1 + e^{\beta(\varepsilon_2+\mu_2)})^{N_{2S}} \quad \text{.....14}$$

As the name implies, the MMTE assumes that the adsorption was carried out on a monolayer with two types of receptor sites, which have two deferent energies (ΔE1 and ΔE2), and that the receptor site can capture a variable number of adsorbate [54]. The change in the adsorbed amount as a function of the equilibrium concentration is given by Eq. 15 [55]:

$$Q_{ads} = \frac{n_{1m}N_{1S}}{1 + (\frac{C_1}{C_e})^{n1m}} + \frac{n_{2m}N_{2S}}{1 + (\frac{C_2}{C_e})^{n2m}} \quad \text{.....15}$$

The adsorption capacity at saturation for MMTE is contingent upon the two types of receptor sites, where it is determined by the summation of Q_{sat1} and Q_{sat2}, as articulated in the subsequent equation:

$$Q_{sat} = Q_{sat1} + Q_{sat2} = n_{1m}N_{1s} + n_{2m}N_{2S} \quad \text{.....16}$$

2.5.3. Double layer model with two energies: DMTE

For this model, the adsorption is carried out in double layers with two energies; the first energy is considered to ensure the solid-liquid interaction (adsorbent-adsorbate) and the second energy to ensure the interaction between the two liquid phases (adsorbate first layer and that of the second layer) [56]. The grand canonical partition function (Zgc) and the one related to the density of receptor sites (Z_{gc}(Ns)) representative of DMTE are given by Eqs. 17 and 18, respectively [57].

$$z_{gc} = 1 + e^{\beta(\varepsilon_1+\mu)} + e^{\beta(\varepsilon_1+\varepsilon_2+2\mu)} \quad \text{.....17}$$

$$Z_{gc}(N_S) = (1 + e^{\beta(\varepsilon_1+\mu)} + e^{\beta(\varepsilon_1+\varepsilon_2+2\mu)})^{N_S} \quad \text{.....18}$$

As a result, the empirical expression of DMTE is given by Eq. 19 [58]:

$$Q_{ads} = n_m N_S \frac{\left(\frac{C_e}{C_1}\right)^{n_m} + 2\left(\frac{C_e}{C_2}\right)^{2n_m}}{1 + \left(\frac{C_e}{C_1}\right)^{n_m} + \left(\frac{C_e}{C_2}\right)^{2n_m}} \quad \text{.....19}$$

Furthermore, the saturation adsorption quantity for this model is determined by Eq. 20:

$$Q_{sat} = 2 * n_m N_S \quad \text{.....20}$$

2.6. Parameters affecting MB adsorption on BOP

In reality, adsorption never occurs in a perfect medium; for example, the adsorption of organic dyes is often sensitive to factors related to the atmosphere and the nature of the medium. To this end, the effects of some parameters were investigated, including the effect of pH, initial concentration, contact time, temperature, ionic strength, and humic acid.

2.6.1. Initial pH effect

The initial pH is an essential factor for understanding the adsorption mechanism. As a consequence, the variance of the adsorbed quantity as a function of the initial pH was examined in a range of 2 to 12 and 50 mg of BOP was put into contact with 50 ml of MB for 48 hours with continuous stirring at 250 rpm. The experiments were repeated three times to ensure the precision of the results and reduce experimental errors.

2.6.2. NaCl and humic acid effects

The inorganic salt NaCl was used as an affecting agent to examine the ionic strength effect for MB adsorption on BOP1 and BOP2. The experimental protocol consisted of a repetition of the adsorption isotherm at 25 °C in the presence of 0.1 mol/L of NaCl. The results obtained were compared to the adsorption isotherm without NaCl. Humic acid (HA) was used to investigate the effect of organic compounds on MB adsorption and the protocol employed was the same as was used for the ionic strength effect.

2.6.3. Temperature effect

In this study, the temperature effect was used to verify the reliability of the adsorption process of MB on BOP. The temperature range was chosen between 10 and 30 °C and the operating conditions were declared in Section 2.4.

2.7. Regeneration study for BOP1 and BOP2

Obtaining regenerable beads was one of this study's goals. Therefore, the regeneration yield of the prepared beads was investigated using a simple protocol that consisted of bringing 200 mg of BOP into contact with 200 ml of MB solution of initial concentration equal to 100 mg/L until equilibrium was reached as described in the adsorption kinetics. Then, the adsorbed dye was desorbed. Due to the fact that methylene blue is a cationic dye, its desorption must be done in an acidic medium. In this study we chose the pH where the adsorption is minimum by employing acidic water (pH=2) with hydrochloric acid (HCL) and the regeneration cycle can be repeated many times until the saturation of beads.

2.8. Material characterization

The distribution of charges on the surface of BOP was characterized by determining the zero charge point (pHpzc) using the protocol described in the literature [59]. Furthermore, the thermal stability of the prepared materials was evaluated using thermogravimetric analysis (TGA) on an SDT Q600 V20.9 Build 20 thermal gravimetric in a temperature range of 30 to 780 °C with a temperature ramping rate of 10 °C/min. Moreover, in the range of 550 to 4000 cm^{-1}, Fourier transform infrared spectroscopy (FTIR) was performed by an Agilent Technologies Fourier Transform Spectrophotometer (FTIR) (Cary 600 series FTIR spectrometer). A Hitachi S-3000N SEM was used to examine the micromorphology (SEM) of the prepared materials. Furthermore, using a ZSX Primus IV-Rigaku, X-ray fluorescence (XRF) was also employed.

2.9. Support Vector Machine

In the 1990s, Vapnik introduced the support vector machine (SVM) [60], which is based on statistical learning theory (SLT) techniques and the concept of structural risk minimization (SRM) [61]. The primary applications of SVM were in non-linear classification and regression analysis [62]. This method involves examining a training dataset of N points (Xi, Yi), with i=1, …, N, where X represents the inputs of the model and Y represents the output. The SVM model is structured as follows:

$$y(x) = \omega^T \phi(x) + b \quad \text{.....21}$$

The function $\phi(.)$: $R^n \rightarrow R^m$ in the given context is a non-linear mapping that transforms the finite dimensional input space into a higher dimensional space that is implicitly generated. Additionally, the weight vector is denoted by ω, and b is the bias term [60,63].

In this research, the experimental data of MB adsorption using two different adsorbents, BOP1 and BOP2, were merged to construct a comprehensive and reliable model for both adsorbents using SVM. The model inputs comprise four variables: contact time (X1) ranging from 0 to 3000 minutes, initial MB concentration (X2) ranging from 50 to 1200 mg/L, pH (X3) ranging from 2 to 12, and temperature (X4) ranging from 10 to 30°C. To differentiate between the adsorbents BOP1 and BOP2, an additional input parameter X5 was introduced, with the values "1" and "2" representing the utilization of BOP1 and BOP2 respectively. The output variable is the MB adsorption capacity (Y).

The optimal SVM model was developed by designing and optimizing the kernel and parameters of SVM.

The process included the following steps [61–64]:

1) The data was prepared and examined.

2) The dataset was divided into three parts: 135 data points were used for training, 28 for evaluating the model's performance (test), and 29 for verifying the model's results (validation).

3) Three kernel functions were used, including Linear, Gaussian, and Polynomial:

- Poly (polynomial)

$k(X_i,X_j) = (ax^T + c)^d$ 22

- Linear

$k(X_i,X_j) = x^T y + c$ 23

- Gaussian

$k(X_i,X_j) = \frac{1}{\sigma\sqrt{2\pi}}\exp\left\{\frac{-X_i - X_j^2}{2\sigma^2}\right\}$ ..... 24 where "c" is the Box constraint, "d" is the Polynomial order, and "σ^2" is the variance in the Gaussian function. These four parameters (d, c, and σ^2) define the kernel functions.

4) The best kernel parameters, such as Box Constraint (1e-3:1e3), Epsilon (0), sigma (1e-3:3), and polynomial order for polynomial kernel (2:5), were obtained through optimization. Optimization algorithms have been utilized to address the problem of trial and error and enhance prediction models to attain superior performance *[65]*. Such algorithms have demonstrated their efficacy in tackling diverse optimization challenges *[66]*. Studies have consistently shown that utilizing optimization algorithms to optimize hyperparameters in machine learning algorithms results in improved performance *[10,11,65–68]*.

In this study, the Lévy flight distribution (LFD) algorithm was integrated with SVM, denoted as SVM_LFD, in order to optimize the kernel function parameters. The LFD algorithm is a stochastic optimization algorithm inspired by the foraging behavior of certain animals, such as birds and fish. It involves random walks with step lengths that follow a probability distribution called the Lévy distribution, which has a heavy tail and allows for occasional long jumps. This new approach was recently introduced in 2021 by Houssein et al. and showed promising results

[65]. By incorporating the LFD algorithm into SVM, it is possible to find the optimal values of kernel parameters more efficiently than manual search. In this study, the number of iterations in the LFD algorithm was set to 100, while the number of search agents was set between 20 and 100.

2.10. Statistical physical modeling evaluation parameters

At the end of the statistical analysis, certain criteria were employed to evaluate the effectiveness of the model. These criteria include the Correlation Coefficient (R), the Coefficient of Determination (R^2), Adjusted Coefficient of Determination (R^2_{adj}), error function (F_{error}), Bayesian Information Criterion (BIC), Root Mean Square Error (RMSE), and Mean Absolute Error (MAE). These values were obtained by applying specific mathematical equations, as follows [10,69–77]:

$$R^2_{adj} = 1 - \frac{(1-R^2)(N-1)}{N-K-1} \quad \text{..... 25}$$

$$F_{error} = \sqrt{\sum_1^N \left(\frac{1}{N-1}\right)\left(\frac{Q_{i,mod}-Q_{i,exp}}{Q_{i,exp}}\right)^2} \quad \text{.....26}$$

$$BIC = K * ln(N) + N * ln\left[\frac{\sum (Q_{e,exp}-Q_{e,mod})^2}{N}\right] \quad \text{.....27}$$

$$RMSE = \sqrt{\left(\frac{1}{N}\right)\left(\sum_{i=1}^{N}\left[\left(y_{\exp} - y_{pred}\right)\right]^2\right)} \quad \text{.....28}$$

$$MSE = \left(\frac{1}{N}\right)\left(\sum_{i=1}^{N}\left(y_{\exp} - y_{pred}\right)^2\right) \quad \text{.....29}$$

$$MAE = \left(\frac{1}{N}\right)\sum_{i=1}^{N}\left|y_{\exp} - y_{pred}\right| \quad \text{.....30}$$

Where $\overline{y}_{exp}$ and y_{pred} are the experimental and the predicted values respectively; $\overline{y}_{exp}$ and $\overline{y}_{pred}$ are the average values of the experimental and the predicted values, respectively [78–81].

3. Results and discussion

3.1. Material characterization

Figure 1 illustrates the isoelectric points of TOP, SA, BOP1, and BOP2. The results indicate a noticeable shift toward alkaline pH in the isoelectric points after encapsulation. This shift is attributed to the formation of "egg box" wherein TOP was surrounded by alginate during beads formation. Notably, BOP2 demonstrates a more acidic nature compared to BOP1, with pHpzc values of 3.3, 5.4, 6.9, and 7.2 for TOP, BOP2, BOP1, and SA, respectively. The micromorphology of TOP, BOP1, and BOP2 is depicted in Figure 2. It is evident from images b-i and c-i that the prepared beads exhibit a spherical shape with slight deformations, likely developed during the drying step. Furthermore, images b-ii, b-iii, b-iv, and c-ii, c-iii, c-iv reveal a heterogeneous dispersion of components and a porous structure, which facilitates and promotes dyes adsorption [82].

The infrared spectra of raw orange peels (ROP), TOP, and encapsulated (BOP1 and BOP2) are shown in Figure 3.

Figure 1. Isoelectric points of TOP, SA, BOP1 and BOP2. (T = 25°C, agitation speed= 250 rpm).

Figure 2. SEM images of TOP (a) [22], BOP1 (b) and BOP2 (c).

Figure 3. Infrared spectra for ROP, TOP, BOP1 and BOP2.

It is evident from these spectra that after acid treatment and encapsulation, some changes occurred: the intensity of some peaks increased, others decreased, and some peaks disappeared. The observed similar peaks are collected in Table 1.

Table1: Wavenumbers (cm^{-1}) of the observed similar peaks from FTIR analysis of ROP, TOP, BOP1 and BOP2.

Suggested attribution	ROP	TOP	BOP1	BOP2	Wavenumber (cm^{-1})
C-O-C stretching [83]	1020	1013	1020	1020	

Cellulosic compounds [29]	1065	1046	1030	1030
C=C of the aromatic rings [84]	1432	1430	1422	1432
C=C and symmetric COO^{--}	1632	1638	1620	1620
$-CH_{Alph}$	2922	2922	2922	2922
−O-H, NH and COOH	3433	3433	3433	3433

The comparison between ROP and TOP spectra leads to the conclusion that phosphoric acid had chemically well modified the structure of ROP. Moreover, the spectra of BOP1 and BOP2 show very similar peaks with small peaks at 1019, 1045, and 1097 cm^{-1}, which can be attributed to the vibration modes of C–O, C–O-H, and C-C on the alginate carbohydrate rings [85].

Thermogravimetric analysis of ROP, TOP, BOP1, and BOP2 was carried out at temperatures ranging from 30 to 780 °C and the obtained curves are shown in Figure 4. These findings show that the loss of water molecules and the degradation of volatile substances [86] occurred between 30 and 200 °C for BOP and between 30 and 230 °C for ROP and TOP. The four materials show thermal stability in these first stages, with mass losses of about 10% for TOP, BOP, and 16% for ROP. The second stage was characterized by an intense mass loss phase between 200 and 400 °C, which may be attributed to the degradation of cellulose [29] on the one hand, and the alginate degradation by breaking its skeleton [87,88] on the other hand. Finally, the last stage was observed between 400 °C and the end of the analysis, characterized by the C-O and C-H bands cracking or by the transformation of the carbonaceous material formed in the previous phases [88,89]. Furthermore, the TGA curves show that the degradation of BOP is less strong compared to ROP and TOP, indicating that the sodium alginate has improved the thermal stability of treated orange peels, and the mass losses are 90.45, 75.91,

74.19, and 74.28 for ROP, TOP, BOP1, and BOP2 respectively. Table 2 shows the results of the XRF analysis of the ROP, TOP, BOP1, and BOP2, with the major compounds listed in percentages. A quick comparison of the phosphorus percentage of the ROP structure shows that it was raised after chemical treatment, which can be attributed to the incorporation of H_3PO_4 in the ROP structure. Otherwise, the presence of chlorine and calcium in the BOP composition confirmed that sodium alginate encapsulation was efficient.

Figure 4. Thermogravimetric analysis of ROP, TOP, BOP 1 and BOP2.

Table 2: XRF analysis of ROP, TOP, BOP1 and BOP2.

Elements (%)	ROP	TOP	BOP1	BOP2
C	48.7	46.5	38.7	40.6
O	50.4	52.7	54.7	54.3
Al	0.046	0.096	0.029	0.036
Si	0.041	0.121	0.044	0.040
P	0.061	0.033	0.009	0.010
Cl	--	--	0.041	0.033
Ca	0.347	0.048	6.22	4.73
Zn	0.038	0.029	0.063	0.071

3.2. Adsorption isotherm

In an adsorption phenomenon, the equilibrium data can be represented as a curve called the adsorption isotherm which can define the adsorbent-dye relationship to provide information on the nature of the adsorption process [90]. Figure 5 illustrates the adsorption isotherms of MB on BOP at different temperatures. These findings indicate that as the temperature rises, the exothermic nature of the adsorption process causes the adsorption potential of MB on BOP to decrease. In addition, for the temperatures 10, 25, and 30 °C, the respective adsorption amounts are 764.92, 612.58, and 508.90 mg/g for BOP1 and 659.78, 523.51, and 400.14 mg/g for BOP2.

Consequently, both materials have good performance. The results obtained from the modeling of adsorption isotherms by applying the Langmuir and Freundlich models are shown in Figure S1. The constants of each model are collected in Table 3. It is clear that the Freundlich model is not appropriate to describe our experimental results. On the other hand, the constants obtained show good determining factors regarding the Langmuir model, but the calculated quantities are a little far from those found experimentally. Consequently, both classical models were not appropriate to describe the experimental results, and hence statistical modeling by using some physical appears relevant.

Material	Modeling	Parameters	10 °C	25 °C	30 °C
BOP1	**Langmuir**	Q_{ads} (mg/g)	764.92	612.58	508.90
		Q_m (mg/g)	816.76	690.54	633.18
		K_L (L/mg)	0.039	0.018	0.009
		R^2	0.996	0.997	0.993
	Freundlich	n_F	3.28	2.81	2.41
		K_F(mg/g)(L/mg)$^{1/n}$	138.93	76.89	43.40
		R^2	0.899	0.928	0.928
BOP2	**Langmuir**	Q_{ads}(mg/g)	659.78	523.51	400.14
		Q_m (mg/g)	739.27	596.39	476.74
		K_L (L/mg)	0.031	0.017	0.012
		R^2	0.997	0.993	0.992
	Freundlich	n_F	3.48	3.08	2.82
		K_F(mg/g)(L/mg)$^{1/n}$	129.64	76.24	46.93
		R^2	0.899	0.928	0.928

Figure 5. MB adsorption isotherms on BOP at varying temperatures. (Agitation speed= 250 rpm, pH=6.2).

Table 3: Langmuir and Freundlich modeling's parameters for MB adsorption on BOP at various temperatures.

3.3. Adsorption kinetics

3.3.1. Initial concentration and time effects

The effect of time and initial concentration of MB adsorption on BOP is investigated and the results are shown in Figure 6. MB adsorption kinetics on both materials (BOP1 and BOP2) are characterized by three stages: (1) a fast phase, (2) a slower second phase, and (3) an equilibrium phase. This can be explained by the availability of active sites at the beginning of adsorption, followed by a progressive reduction in the number of free sites until saturation [80]. Furthermore, the amount of MB adsorbed increases as the initial concentration increases, which can be related to the driving force [91]. The amounts adsorbed at equilibrium were 45.94, 91.62, and 182.04 mg/g for BOP1 and 46.21, 91.44, and 181.14 mg/g for BOP2 for initial concentrations of 50, 100, and 200 mg/L, respectively. Therefore, these kinetics results were modeled using PFO, PSO, and PNO models, and the curves obtained are shown in Figure 6, and the corresponding constants are summarized in Table 4. The best-model selection is typically based on a variety of criteria, such as the coefficient of determination R^2 (the model

is more suitable if R^2 is closer to 1), the gap between the experimental and model-calculated adsorbed quantities, as well as the error function's calculated values (the model is more suitable if F_{error} is closer to 0). As a result, all used models demonstrate that the adsorbed quantities are similar to those found experimentally, regardless of the initial concentrations. Moreover, Table 4 shows that the PFO and PNO models have high determination coefficients and low F_{error} values compared to the PSO model. The PNO model provided parameter values "n" that were very close to 1. So, it can be assumed that the PFO model is the most relevant to describe experimental data.

In addition, Figure 7 shows that for both beads and whatever the initial concentration, the curves of the intraparticle model show three lines which do not pass through the origin (intercepts ≠ 0). These three lines indicate that the process of MB adsorption on BOP occurred in different phases, of which the second line illustrates intraparticle diffusion which, however, is not the limiting step [92]. Therefore it can be assumed that the final stages of adsorption were controlled by film diffusion [93]. Figure 8 illustrates the results obtained from the Boyd modeling, showing linear points during the first minutes of adsorption for the two materials (BOP1 and BOP2), but they do not pass through the origin. Overall, the data were not linear, suggesting that film diffusion was the limiting step rather than pore diffusion [94]. The above interpretation is compatible with the intraparticle model assumption.

Figure 6. Time and initial concentration effects (symbols), and PFO, PSO and PNO modeling curves (continuous lines) for MB adsorption onto BOP1 and BOP2. (T = 25°C, agitation speed= 250 rpm, pH=6.2).

Table 4: Parameters of PFO, PSO, PNO, Intraparticle and Boyd models for MB adsorption onto BOP1 and BOP2.

Material	Model	Parameters	C_0(mg/L)		
			50	**100**	**150**
BOP1	**PFO**	Q_{ads} (mg/g)	45.94	91.62	182.04
		Q_{mod} (mg/g)	43.92	91.18	180.86
		$K_{1.}$ (min^{-1})	0.009	0.007	0.006
		R^2	0.982	0.989	0.999
		F error	0.0109	0.0012	0.0016
	PSO	Q_{mod} (mg/g)	46.86	97.67	195.04
		$K_2.*10^4$ (gm g^{-1} min^{-1})	2.95	1.02	0.14
		R^2	0.943	0.960	0.990
		F error	0.0112	0.0165	0.0178
	PNO	Q_{mod} (mg/g)	43.89	91.12	181.28
		$k_{n.}$ (min-1) $(mg\ g^{-1})^{1-n}$	0.010	0.008	0.003
		N	0.962	0.950	1.102
		R^2	0.984	0.990	0.999
		F error	0.0111	0.0013	0.001
	Intraparticle (First step)	K_{id} (mg g^{-1} $min^{-0.5}$)	4.17	6.42	10.64
		I (mg g^{-1})	- 15.99	- 18.98	-27.60
		R^2	0.98827	0.996	0.991
	Intraparticle (Second step)	K_{id} (mg g^{-1} $min^{-0.5}$)	2.12	2.02	1.62
		I (mg g^{-1})	6.50	44.08	117.13
		R^2	0.987	0.991	0.958
BOP2	**PFO**	Q_{ads} (mg/g)	46.21	91.44	181.14
		Q_{mod} (mg/g)	43.95	89.21	180.18
		$K_{1.}$ (min^{-1})	0.009	0.008	0.006
		R^2	0.984	0.996	0.997
		F error	0.0122	0.0061	0.0013
	PSO	Q_{mod} (mg/g)	46.98	95.04	192.70
		K_2*10^4 (gmg^{-1} min^{-1})	2.81	1.31	0.50
		R^2	0.936	0.972	0.993
		F error	0.0149	0.0098	0.0159
	PNO	Q_{mod} (mg g^{-1})	43.93	89.09	181.81
		$k_{n.}$ (min-1) $(mg\ g^{-1})^{1-n}$	0.011	0.009	0.002
		N	0.961	0.958	1.288
		R^2	0.980	0.996	0.999
		F error	0.0123	0.0064	0.0009
	Intraparticle (first step)	K_{id} (mg g^{-1} $min^{-0.5}$)	3.48	5.86	10.06
		I (mg g^{-1})	-11.24	-10.72	-13.67
		R2	0.969	0.986	0.993
	Intraparticle	K_{id} (mg g^{-1} $min^{-0.5}$)	0.06	0.31	1.32

(Second step)	I (mg g^{-1})	39.73	74.83	129.05
	R^2	0.805	0.959	0.999

Figure 7. Intraparticle model for MB adsorption onto BOP1 and BOP2 at different initial concentrations. (T= 25 °C, Agitation speed= 250 rpm, pH=6.2).

Figure 8. Boyd model for MB adsorption onto BOP2 and BOP2 at different initial concentrations. (T= 25 °C, agitation speed= 250 rpm, pH=6.2).

3.4. pH effect

Figure 9 illustrates the initial pH effect for MB adsorption on BOP1 and BOP2. The two materials display the same shape, with curves divided into three stages. The first one is seen between pH 2 and 4, where the yield rises from 20 to 93.18 % for BOP1 and from 11 to 92.88 % for BOP2. This low yield in acidic pH is likely due to electrostatic repulsion between the positive charges of the MB dye and those of the adsorbent. The second stage is observed between pH 4 and 10, where the adsorption quantity is quite good and almost constant for both beads and this behavior is attributed to the presence of negative charges as the pH tends towards alkaline values [95]. Finally, the last stage between pH 10 and 12 is characterized by a slight decrease in yield due to MB structure modification in this interval, where the maximum wavelength shifted from 654 to 550 nm.

Figure 9. Initial pH effect for MB adsorption onto BOP1 and BOP2. (T = 25°C, agitation speed= 250 rpm).

3.5. NaCl and humic acid presence effect

Figure 10 illustrates the behavior of MB adsorption in the presence of NaCl or HA. The findings show that when NaCl was added, the adsorption capacity of MB decreased because of dissolution of NaCl into Na^+ and Cl^-, which induces, on one hand, a competitive adsorption between the Na^+ cations and the MB molecules and, on the other hand, the neutralization of the MB molecules by the Cl^- ions [96]. Contrarily, the addition of HA had no effect on the adsorption performance of MB on the two materials, as seen in Figure 10.

Figure 10. NaCl and HA presence effects for MB adsorption onto BOP1 and BOP2 at 25°C. (Agitation speed= 250 rpm, pH=6.2).

3.6. Reuse of prepared beads

The regeneration tests of BOP1 and BOP2 (Figure 11) indicate a remarkable reusability efficiency since the adsorption cycles can be repeated more than 7 times without a significant decrease in the adsorption yield. Indeed, the adsorption decreases are 5.93 % and 8.23% for BOP1 and BOP2 respectively between the first and the seventh cycles, indicating a slightly higher efficiency for BOP1.

Figure 11. Regeneration efficiency of BOP1 and BOP2 at 25°C. (T = 25°C, agitation speed= 250 rpm, pH=2).

3.7. Statistical physical modeling

In this section, the adsorption isotherms modeling is performed using statistical physics models. As a consequence, to explain the mechanism of adsorption at the molecular level, adequate model parameters are considered to calculate, plot, and interpret thermodynamic functions such as free enthalpy, entropy, and internal energy.

3.7.1. Choosing the best model

The curves obtained from the used statistical models, namely MMSE, MMTE and DMTE, are presented in Figure 12. The adjusted determination coefficient R^2, F_{error} function, and the Bayesian information criterion (BIC) values obtained from each model are summarized in Table 5.

Figure 12. MMSE, MMTE, and DMTE modeling curves for MB adsorption isotherms onto BOP1 and BOP2 at different temperatures. (Agitation speed= 250 rpm, pH=6.2).

Table 5: The performance measures of the used statistical physics models.

Material	Models	10°C			25°C			30°C		
		R^2	F_{error} (%)	BIC	R^2	F_{error} (%)	BIC	R^2	F_{error} (%)	BIC
BOP1	MMSE	0.99669	0.02377	79.66	0.9977	0.05047	67.28	0.99533	0.0278	62.26
	MMTE	0.99935	0.00156	66.21	0.99945	0.03460	56.41	0.99936	0.01685	47.61
	DMTE	0.99900	0.13977	69.77	0.99805	0.11868	67.67	0.99654	0.13368	61.36
BOP2	MMSE	0.99757	0.02207	77.15	0.99288	0.04412	83.46	0.99289	0.04001	65.77
	MMTE	0.99957	0.00768	60.72	0.99886	0.00974	65.79	0.99908	0.01785	48.71
	DMTE	0.99757	0.02221	76.03	0.99412	0.11576	83.42	0.9929	0.13063	65.45

It is clear that the three models provided excellent adjusted coefficients of determination (R^2). Table 5 also shows that for the two materials, the second model, MMTE, offered the lowest F_{error} and BIC values. As a result, it can be considered that the MMTE is the most suitable model for describing the experiment results.

3.7.2. Steric interpretation for the adequate model (MMTE)

The n_{im} is one of the parameters that are essential in understanding the adsorption process since it can describe the orientation of the adsorbed molecule on the adsorbent surface [97]. As a result, three scenarios can be considered. First, if n_{im} is less than 0.5, the adsorption occurs through a multi-interaction mechanism, i.e. the MB molecule can be adsorbed on at least two

free adsorption sites [98]. Otherwise, the MB molecule can be adsorbed on a single and two free adsorption sites simultaneously with random and different probabilities in the second scenario if n_{im} is between 0.5 and 1 [27,28]. It is worth noting that the n_{im} in the first two scenarios means that the adsorbate molecules were adsorbed parallel to the adsorbent surface [99]. In the third scenario, where n_{im} equals or exceeds 1, the adsorbate molecule is captured at a single adsorption site with an inclined or perpendicular orientation to the adsorbent surface [99,100]. Table 6 shows the variation of n_{1m} and n_{2m} as a function of temperature. These results indicate that for both materials and whatever the temperature n_{2m} is greater than n_{1m}. Furthermore, n_{1m} has variable values ranging from 0.66 to 1.48, indicating that the MB molecules adsorption occurs in diverse types. To better understand these findings, two cases are considered in the following.

The first case (BOP1 at 10 °C; BOP2 at 10 and 25 °C) with n_{1m} and n_{2m} both greater than 1: the MB molecules were adsorbed on a single site with an inclined or perpendicular orientation to the BOP surface. The second case (BOP1 at 25 and 30; BOP2 at 30 °C): the MB molecules were adsorbed simultaneously on a single and two free sites with mixed positions (parallel and perpendicular). From these results, the MB adsorption on a single free site in an inclined or perpendicular position is the dominant mode. Furthermore, physical statistical models provide more accurate values for the amount adsorbed at saturation Q_{sat}. As is well known, Q_{sat} is described by the density of the receptor sites (Nis) multiplied by n_{im}. It reflects BOP's ability to absorb MB. In the case of MMTE, the total Q_{sat} is given by the sum of Q_{sat1} and Q_{sat2}. The total Qsat for each material at different temperatures are shown in Table 6 and the obtained results demonstrate that the model's Q_{sat} values agree with Q_{ads}. Table 6 also indicates that total Q_{sat} decreases with the temperature, suggesting that the mechanism of MB adsorption on BOP is exothermic.

Table 6: Obtained parameters of the best model (MMTE) for MB isotherm adsorption onto BOP1 and BOP2 at different temperatures.

	T (°C)	n_{1m}	N_1s (mg/g)	n_{2m}	N_{2s} (mg/g)	C_1 (mg/L)	C_2 (mg/L)	Q_{sat1} (mg/g)	Q_{sat2} (mg/g)	$Q_{sat\ totale}$ (mg/g)	Q_{ads} (mg/g)	R^2	F error (%)	BIC
BOP1	10	1.48	346.03	2.29	117.91	10.52	93.11	511.77	269.41	781.19	764.92	0.999	0.00156	66.21
	25	0.89	658.44	3.54	25.46	44.83	97.40	587.33	90.31	677.63	612.58	0.999	0.0346	56.41
	30	0.66	131.13	1.63	278.78	5.05	92.69	86.55	455.80	542.35	508.90	0.999	0.01685	47.61
BOP2	10	1.03	221.26	1.55	301.31	6.68	46.70	277.83	468.22	696.05	659.78	0.999	0.00768	60.72
	25	1.05	160.36	1.78	210.23	6.82	80.77	168.53	373.37	541.90	523.51	0.999	0.00974	65.79
	30	0.74	80.37	1.57	231.54	1.37	87.08	59.39	346.44	423.83	400.14	0.999	0.01785	48.71

3.7.3. Energetic interpretations

The system's adsorption energy is a crucial parameter for determining the type of interactions that occur during the process; this adsorption energy can be calculated using the following relationships (Eqs. 31 and 32) [45]:

$$C_i = C_S e^{\frac{-\Delta E_i}{RT}} \quad \text{.....31}$$

$$\Delta E_i = -RT ln\left(\frac{C_i}{C_S}\right) \quad \text{.....32}$$

Table 7 summarizes the results of the MB adsorption energies calculations on BOP1 and BOP2 at different temperatures. This table indicates that for the two materials, ΔE1 is always greater than ΔE2, indicating that the first type of free active site is the most dominant. Moreover, the negative values signify that the interactions between the MB and BOP were exothermic. Based on the literature, the calculations carried out show that for the two materials, the values of E_{ad} of MB were <40 kJ/mol, indicating the physisorption of the process [101] employing electrostatic interactions, hydrogen bonding, and hydrophobic interactions π-π [48].

Table 7: Calculated adsorption energies from MMSE model for MB adsorption onto BOP1 and BOP2 at different temperatures.

Material	T (° C)	ΔE1 (kJ/mol)	ΔE2 (kJ/mol)
BOP1	10	-19.39	-13.76
	25	-16.83	--13.66
	30	-22.61	-13.77
BOP2	10	-20.46	-15.33
	25	-21.49	-14.08
	30	-25.90	-13.91

3.7.4. Thermodynamic function calculation

The best statistical physic model (MMTE) parameters are used to conduct the calculations required to measure and plot the internal energy, Gibbs free enthalpy, and configuration entropy

to perform a thermodynamic study of the MB adsorption mechanism on the two materials (BOP1 and BOP2).

3.7.4.1. Entropy

Evaluating an adsorption system's entropy configuration may provide valuable information about the order and disorder of the adsorbate. The relationship given by Eq. 33 is obtained by combining the grand canonical partition function Zgc with the large statistical potential (J) [57].

$$J = -k_B T ln Z_{gc} = -\frac{\partial ln Z_{gc}}{\partial \beta} - TS_a \quad \text{.....33}$$

As a result, Eq. 30 provides the following relationship (Eq. 34) [57]:

$$\frac{S_a}{k_B} = -\frac{\beta \partial Ln Z_{gc}}{\partial \beta} + ln Z_{gc} \quad \text{.....34}$$

As a consequence, the second model's entropy variation as a function of the adsorbate equilibrium concentration is given by Eq. 35 [102] :

$$\frac{S_a}{k_B} = N_{1S}\left[ln\left(1+\left(\frac{C_e}{C_1}\right)^{n_{1m}}\right) + \frac{n_{1m} ln\left(\frac{C_1}{C_e}\right)}{1+\left(\frac{C_1}{C_e}\right)^{n_{1m}}}\right] + N_{2S}\left[ln\left(1+\left(\frac{C_e}{C_2}\right)^{n_{2m}}\right) + \frac{n_{2m} ln\left(\frac{C_2}{C_e}\right)}{1+\left(\frac{C_2}{C_e}\right)^{n_{2m}}}\right] \quad \text{.....35}$$

Figure 13 illustrates the evolution of entropy as a function of the equilibrium concentration. The two materials provide similar curves that can be separated into two parts: the first part is observed at low concentrations where entropy increases while the second part is seen at high concentrations where entropy decreases. This can be explained as follows: at low concentrations, MB molecules have a variety of opportunities for choosing free active sites to adsorb onto them, which leads to more disorder. However, at high concentrations, the BOP surface tends to monolayer saturation, which means that MB molecules do not have as many opportunities for being adsorbed, so the choice of free active sites is limited resulting in reduction in the disorder [103]. In general, when equilibrium is achieved, the entropy tends to

zero [104], but this is not the case in our analysis, indicating that saturation has not yet been reached [105].

Figure 13. The evolution of entropy as a function of equilibrium MB concentrations at different temperatures for BOP1 and BOP2.

3.7.4.2. Gibbs free enthalpy

As it is known, the spontaneity of adsorption is determined by the Gibbs free enthalpy, which is presented by Eq. 36 [48] :

$$G = \mu Q \quad \text{.....36}$$

Where the chemical potential is given by Eq. 37 [106]:

$$\mu = k_B T ln\left(\frac{N_s}{Z_{tr}}\right) \quad \text{.....37}$$

Then, the Gibbs free enthalpy for MMTE expression is given by Eq. 38 [107]:

$$G = k_B T ln\left(\frac{C_e}{Z_v}\right)\left[\frac{Q_{sat1}}{1+\left(\frac{C_1}{C_e}\right)^{n_{1m}}} + \frac{Q_{sat2}}{1+\left(\frac{C_2}{C_e}\right)^{n_{2m}}}\right] \quad \text{.....38}$$

Figure 14 shows the results of the Gibbs free enthalpy calculations as a function of MB concentrations at different temperatures. These results indicate that G values are negative regardless of the temperature, confirming the thermodynamic adsorption spontaneity of MB onto BOP1 and BOP2 [107]. Figure 14 also shows that the MB adsorption feasibility decreases with rising temperature [101], which is likely due to the reduction of thermal collisions number [108].

Figure 14. Gibbs free enthalpy variation as a function of equilibrium MB concentrations at different temperatures for BOP1 and BOP2.

3.7.4.3. Internal energy

The energy of an adsorption system can be described as a fundamental concept developed to quantify the nature of interactions between its various components (including adsorbate-adsorbate interactions) so that it can express any type of energy that may occur in the process [103]. Therefore, internal energy is a key parameter for understanding the physical and chemical phenomena in this system.

The general equation of the internal energy can be described using the canonical grand partition function as follows [3] :

$$E_{int} = -\frac{\partial ln(Z_{gc})}{\partial \beta} + \frac{\mu \partial ln(Z_{gc})}{\beta \partial \mu} \quad \text{.....39}$$

Finally, the internal energy function for the monolayer model with two energies (MMTE) is given by Eq. 40 [102]:

$$E_{int} = k_B T \left[N_{1s} \frac{ln(\frac{C_e}{Z_v}) + n_{1m} ln(\frac{C_1}{C_e})}{1 + (\frac{C_1}{C_e})^{n_{1m}}} + N_{2s} \frac{ln(\frac{C_e}{Z_v}) + n_{2m} ln(\frac{C_2}{C_e})}{1 + (\frac{C_2}{C_e})^{n_{2m}}} \right] \quad \text{.....40}$$

Therefore, E_{int}/k_BT is plotted as a function of Ce in Figure 15.

Figure 15. Internal energy variation as a function of equilibrium MB concentrations at different temperatures for BOP1 and BOP2.

It is clear that the values of E_{int} of the two materials are negatives, confirming the process spontaneous nature [26] (in agreement with the results of Gibbs free enthalpy). Furthermore, the E_{int} values obtained can be divided into two cases. For low concentrations, the absolute values of the internal energies vary randomly with the rise of temperature. In contrast, in the second case, the absolute values of internal energies decrease with increasing temperature, possibly due to a decrease in the thermal collisions number [109]. The two cases suggest the presence of exothermic and endothermic (at the first adsorption moments) adsorption stages [102].

4. Proposed mechanism for MB adsorption on BOP

As a result of all the obtained findings, it can be assumed that MB adsorption on BOP is spontaneous and exothermic [26], as demonstrated by the Gibbs free enthalpy and internal energy functions. Moreover, the physisorption of the process indicates that its mechanism can be achieved through electrostatic interactions and hydrogen bonding. This bonding can occur between the electronegative nitrogen (N) atom of the MB dye and the –COOH and –OH functional groups of the alginate [110]. Additionally, there is a contribution from hydrophobic interactions π-π between the aromatic rings in MB and those of BOP [111]. Note that π-π interactions primarily originate from TOP due to its cellulosic form as found in our previous study [29]. Furthermore, the n_{im} parameter proved that MB molecules were adsorbed by a mixed monolayer with various orientations, namely perpendicular and horizontal, on a single and two free sites at the same time, but with a dominance of MB adsorption on a single free site under an inclined position to the BOP surface [28,98,99]. It is important to point out that the contribution of TOP on MB adsorption was limited compared to its powder state, as found in our previous study [29]. This finding can be attributed to the formation of the "egg box" as mentioned in Section 2.2 [30], wherein TOP was surrounded by alginate. Consequently, it contributed to the MB adsorption mechanism, but in a limited way. Figure 16 summarizes everything that was said about the adsorption mechanism of MB on BOP.

Figure 16. Proposed mechanism for MB adsorption onto BOP.

5. Support Vector Machine coupled with Levy Flight Distribution Optimization

In this section, three kernel functions are optimized using the LFD algorithm. The linear, Gaussian, and polynomial kernels mentioned in Section 2.9 are used. After obtaining the results of the learning phase, the SVM model was validated using the validation database. The predicted values generated by the model were compared to the experimental values in the

training and validation phases to calculate R, R^2, R^2_{adj}, RMSE, MSE, EPM, ESP and MAE. The results of these tests showed that the Gaussian kernel function represented the best result compared to the other kernels. This result is shown in Table 8.

Table 8: Performances of SVM_LFD Kernel function.

LFD Max_iteration=100 SearchAgents_no=40										
Kernel function	***c***	***E***	**σ^2**	**Quantity of support Vectors**	**R/R^2/R^2_{adj}**			**RMSE/MAE**		
					Train	**Val**	**All**	**Train**	**Val**	**All**
Gaussian	**1910**	**1.6000**	**7.2404**	**135**	**0.9981 0.9962 0.9960**	**0.9973 0.9945 0.9934**	**0.9985 0.9970 0.9970**	**12.0832 5.3954**	**7.9200 6.9612**	**11.1425 5.7929**

The optimal parameters of the Gaussian kernel function were found using the LFD method with a maximum number of iterations of 100 and the number of "search agents" as 40. This search approach of parameters made it possible to optimize the performance of the model by finding the ideal values for C, ε and σ^2. The values of these parameters have been selected so as to minimize the mean squared prediction errors, equivalent to maximize the coefficient of determination R^2.

The model parameters for the Gaussian kernel function found by the LFD method are as follows: C = 1910, ε = 1.6 and σ^2 = 7.2404 and they produced very satisfactory prediction performance for the three sets of data: training, validation and the complete data (all data). Indeed, for the training phase the coefficients of R, R^2 and R^2_{adj} have values of 0.9981, 0.9962, and 0.9960 respectively indicating that the model almost perfectly explains the variance of the training data. Prediction errors are also very low, with an RMSE of 12.0832 and an MAE of 5.3954. These results indicate that the model is able to fit the training data well and provide accurate predictions. For the validation phase, the values of R, R^2 and R^2_{adj}

are slightly lower at 0.9973, 0.9945 and 0.9934 respectively, but remain high and indicate good generalization capacity of the model. The prediction errors are slightly higher than in the training phase, with an RMSE of 7.9200 and an MAE of 6.9612, but remain relatively low compared to the amplitude of the data. Finally, for "all data", the coefficient of determination R^2 is even higher with a value of 0.9970, confirming the model's ability to generalize and adapt to complete data. The values of R and R^2_{adj} are also very high, with respective values of 0.9985 and 0.9970, confirming the reliability and accuracy of the model. Prediction errors are also very low, with an RMSE of 11.1425 and MAE of 5.7929, indicating that the model is capable of producing accurate predictions even on new data.

The results obtained indicate that the model using the Gaussian kernel function with the specified parameters is able to fit the training data well, to generalize on the validation data and to provide accurate predictions on the full data.

This result was represented graphically (Figure 17) in terms of the experimental values and the predicted values.

Figure 17. Relationship between the experimental and the SVM-LFD model predicted values.

5.1. Model performance test

Model performance results for generalization were evaluated using a cached database comprising 28 experimental data points that were not used during model development. The performance results are presented in Table 9, which shows the values of R, R^2 and R^2_{adj}, as well as the statistical errors (RMSE and MAE).

Table 9: Model test performance.

R	R^2	R^2_{adj}	RMSE	MAE
0.9989	0.9978	0.9972	9.0789	6.4998

The results show that the generated SVM-LFD model has good generalization, with a coefficient of determination R^2 of 0.9989, indicating a very good generalization capacity of the model. The values of R and R^2_{adj} are also very high, with respective values of 0.9989 and 0.9972, confirming the reliability and accuracy of the model.

As far as statistical errors are concerned, the values are also very low, with an RMSE of 9.0789, and an MAE of 6.4998. These values indicate that the model is capable of providing very accurate predictions for the additional unseen testing data.

The results obtained for the performance of the model for the generalization tests are very satisfactory, with high values for the coefficients of determination and very low statistical errors. This confirms the efficiency and accuracy of the generated SVM-LFD model to predict complex phenomena in various scientific fields.

This result is represented graphically in Figure 18 in terms of the experimental values and the predicted values.

Figure 18. Comparison between experimental and predicted values to assess performance.

5.2. Residues study

The residual analysis approach is used in this study to investigate the efficiency and performance of the chosen model [61,78]. The experimental and predicted values are plotted together against samples in Fig. 19(a) for all data (including training, validation and test data) [74,79].

The model prediction errors are plotted as time series in Fig. 19(b). The distributions of model prediction errors are plotted as histograms in Fig. 19(c) and Fig. 19(d) [61].

Figure 19.a shows the exceptional close matching between the actual values and the estimated values for the three sets of data (training, testing and validation), indicating the high accuracy of the developed model. Figure 19.b displays very small errors in the range of [-25 to 25] for all three data sets (except two errors that exceeded this range), with the majority of errors clustered around zero. This highlights the robustness and accuracy of the model. Figure 19.c shows a notable high proportion of errors around 0 for all three data sets. This means that the model was able to accurately predict the values for a significant proportion of the samples. This is further reinforced by Figure 19.d, which displays a high frequency of errors around 0 (close to 100 occurrences), indicating the efficiency and effectiveness of the developed model. Overall, these results suggest that the developed model is able to accurately predict the expected values with high accuracy, making it a reliable tool for future studies in this area.

Figure 19. Residuals relating to the model established by the different techniques according to the estimated values: (a) experimental data and the predicted data against samples, (b) model errors against samples, (c) histogram of all errors, and (d) histograms of errors on training, testing, and validation data sets.

5.3. Optimization and validation of the optimum conditions

The LFD approach was utilized to find the optimal process condition for achieving maximum MB uptake with both adsorbents. The four decision variables are: X1 (contact time), X2 (initial MB concentration), X3 (pH), and X4 (temperature). After the optimization process, laboratory experiments were conducted to validate the optimization result. Table 10 displays the comparison between the predicted and experimental outcomes, as well as the corresponding errors for each adsorbent.

Where: $Error = Experimental\ response - Predicted\ response$ ……41

Table 10: Comparison between actual and predicted responses at optimum conditions.

BOP1 LFD: X1 = 2833 min, X2 = 1200 mg/L, X3 = 5.9, and X4= 10°C	
Predicted MB uptake (mg/g)	753.7781
Experimental MB uptake (mg/g) values	764,9165
Error (mg/g)	11,1384
BOP2 **LFD: X1 = 2797 min, X2 = 1200 mg/L, X3 = 6.5, and X4= 10°C**	
Predicted MB uptake (mg/g)	641.3378
Experimental MB uptake (mg/g) values	659,7792
Error (mg/g)	18.4414

For BOP1, the optimal conditions were determined to be X1=2833 min, X2=1200 mg/L, X3=5.9, and X4=10°C, with an expected MB uptake of 753.7781 mg/g. Laboratory experiments were conducted to validate these conditions, and the actual absorption of MB was found to be 764.9165 mg/g. The error between the predicted and experimental values was 11.1384 mg/g, indicating that the LFD method was successful in determining the optimal conditions for maximum MB uptake in BOP1. Similarly, for BOP2, the LFD method was used to determine the optimal conditions for maximum MB uptake, which were found to be X1 = 2797 min, X2 = 1200 mg/L, X3 = 6.2, and X4 = 10°C, with a predicted MB absorption of 641.3378 mg/g. Laboratory experiments were conducted to validate these conditions, and the actual MB absorption was measured at 659.7792 mg/g, resulting in an error of 18.4414 mg/g.

The errors shown in Table 10 indicate that the SVM_LFD model is effective in predicting MB uptake in BOP1 and BOP2 samples and in optimizing process conditions for achieving maximal MB removal.

5.4. User interface for optimization and prediction

A sophisticated software tailored for the Windows operating system has been meticulously designed to enhance the optimization and predictive capabilities of MB adsorption for two distinct adsorbents, as visually depicted in Figure 20. This intuitively user-friendly application seamlessly consolidates and enriches all the intricate calculations conducted in the course of this investigation. This software enables users to effortlessly predict and optimize MB adsorption with enhanced precision and efficiency.

The initiation of this application unfolds smoothly and intuitively, providing an optimal user experience. In the upper section, the integration of the LFD algorithm aims to determine the optimal conditions (X1, X2, X3, X4) based on the previously developed SVM_LFD model. To do so, the user starts by selecting the adsorbent of their choice, indicating the corresponding number in the ‘’Type of adsorbent’’ box: 1 for BOP1 and 2 for BOP2. Subsequently, it is necessary to define the search interval for each parameter by specifying the lower bound (LB) and upper bound (UB). Once these steps are completed, the optimization process is initiated with a simple click on the "LFD" button, obtaining the optimal parameters that maximize the adsorbed quantity for each material.

In the prediction section, determining the adsorbed quantity for each material is simplified. The user only needs to choose the adsorbent by entering 1 for BOP1 or 2 for BOP2. Then, it is a matter of inputting the values of X1, X2, X3, and X4, and launching SVM_LFD to predict the adsorbed quantity for the selected material. All of these steps are clearly outlined in Figure 20, facilitating a quick and comprehensive understanding of the application's usage process.

This user-friendly application, equipped with its ability to optimize and predict, serves as a valuable asset in the field of adsorption studies.

Figure 20. MATLAB user interface for optimization and prediction of MB uptake using SVM_LFD.

6. Comparison of the adsorption performances of BOP1 and BOP2 with other adsorbents

The adsorption performance of BOP1 and BOP2 under optimal conditions is compared with other adsorbents reported in the literature and the results are given in Table 11.

Precursor	Biopolymer	Pollutant	Adsorbed quantity (mg/g)	pH	T (°C)	Maximum pollutant concentration (mg/L)	References
Rice husk	Alginate	MB	274.9	6	20	500	[25]
Montmorillonite nanosheets	Alginate	MB	564.97	8	25	300	[112]
Cellulose nanocrystals	Alginate	MB	676.7	7	25	1600	[113]
Coffee grounds /cellulose	Alginate	MB Congo red	397.76 397.14	6 2	25 25	400 400	[114]
Montmorillonite	Chitosane	Methyl green	396.19	6	25	500	[115]
Cellulose	Alginate	MB	38	7	30	100	[116]
BOP1	Alginate	MB	764.92	5.9	10	1200	This study
BOP2	Alginate	MB	659.78	6.2	10	1200	This study

Table 11: The adsorption performances of BOP1 and BOP2 in comparison with other adsorbents.

It can be seen from Table 11 that rice husk combined with alginate demonstrates an adsorption capacity of 274.9 mg/g for MB at pH of 6 and temperature of 20°C. Similarly, montmorillonite nanosheets combined with alginate exhibit an adsorption capacity of 564.97 mg/g for MB, with pH of 8 and temperature of 25°C. Cellulose crystals, when paired with alginate, showcase a

noteworthy adsorption capacity of 676.7 mg/g for MB at pH of 7 and temperature of 25°C. Among other observations, coffee grounds and cellulose demonstrate adsorption capacities for both MB and Congo Red, with respective adsorbed quantities of 397.76 mg/g and 397.14 mg/g. Lastly, within our study, materials BOP1 and BOP2 exhibit remarkable adsorption capacities for MB, reaching 764.92 mg/g and 659.78 mg/g, respectively, at pH values of 5.9 and 6.2, and temperature of 10°C. These results significantly highlight the variability in the effectiveness of our materials under specific adsorption conditions, promising avenues for the treatment of diverse pollutants.

7. Conclusion

The study demonstrates the potential of orange peels as an effective precursor for synthesizing sodium alginate-encapsulated beads for the removal of methylene blue (MB) from aqueous solutions. The experimental data for adsorption kinetics is analyzed using various models, and the PFO model is found to be the most appropriate for describing the data. Furthermore, the Boyd and intraparticle models suggest that the limiting step is the diffusion of films. The adsorption isotherms are best described by the MMTE model, which indicates that the adsorption of MB on the prepared beads occurs through a mixed monolayer process. The regenerated beads could be reused up to seven cycles, indicating their potential for practical applications. The study also shows that NaCl inhibits MB adsorption due to competition with Na+, while humic acid has no effect on the adsorption process. The thermodynamic study reveals that the adsorption process is spontaneous and exothermic, and the availability of free active sites on the BOP surface is related to the order and disorder of the system. The findings of this study suggest that orange peels can be a low-cost and environmentally friendly precursor for synthesizing sodium alginate-encapsulated beads for wastewater treatment applications.

Finally, the SVM-LFD model is found to be highly accurate with minimal statistical errors and is effective in predicting the adsorption behavior of the prepared beads. This model is a promising tool for predicting the performance of similar adsorbents and optimizing their design for practical applications. This study presents a comprehensive investigation of the potential use of orange peels as a precursor for synthesizing sodium alginate-encapsulated beads for wastewater treatment applications. The findings of this study contribute to the development of effective and sustainable adsorbents for the removal of pollutants from aqueous solutions.

8. Nomenclatures

BOP	Beads of orange peels.
BOP1	Beads of orange peels with a TOP-SA ratio equal to 1.
BOP2	Beads of orange peels with a TOP-SA ratio equal to 2.
C	Box Constraint
C_0	MB initial concentration (mg/L).
C_1, C_2, $C_{1/2}$	Concentrations at half-saturation of the adsorbed layer (mg/L).
C_e	MB concentration at equilibrium (mg/L).
C_S	MB solubility (g/L).
C_t	MB concentration at time t (mg/L).
E_{int}	System internal energy (J/mol)
G	Gibbs free enthalpy function (J/mol)
h	Planck constant (J/s).
K	The number of variables (inputs).

I	Intraparticle model constant (mg/g).
K_B	Boltzmann constant (J/K).
K_F	Constant of Freundlich model (mg L/g).
K_{id}	Constant of diffusion rate from intraparticle model (mg/g $min^{-0.5}$).
K_L	Constant of Langmuir model (L/mg).
K_n	The rate constant of PNO. (min^{-1}) (mg $g^{-1})^{1-n}$
K_1	The rate constant of PFO (1/min).
K_2	The rate constant of PSO (g/(mg min)).
m	Adsorbent mass (g).
N	The number of data samples.
N_{iS}	Density of (i) Receptor sites (mg/g).
n	Sorption reaction order.
n_f	Heterogeneity index of the Freundlich model.
n_{im}	The number of MB molecules captured by the receptor sites.
PFO	Pseudo first order model.
PSO	Pseudo second order model.
PNO	Pseudo nth order model.
Q_e	Equilibrium adsorbed quantity (mg/g).
Q_m	Adsorbed quantity of one layer for Langmuir model (mg/g).
Q_{mod}	Adsorbed quantity obtained by the kinetic models (mg/g).
Q_{sat}	Adsorbed quantity at saturation (mg/g).
Q_{ads}	Adsorbed quantity (mg/g).
ROP	Raw orange peels.
R_E	BOP regeneration efficiency (%).
R^2	determination coefficient.

SA	Sodium alginate.
Sa	Entropy configuration (J/mol K)
T	Temperature (°C or K).
t	Time (min).
TOP	Treated orange peels.
V	Volume (L).
Z_v	Translation partition function per unit volume.
z_{gc}	The grand canonical partition function of one site.
Z_{gtr}	The translation partition function.
$Z_{gc}(N_S)$	The grand canonical partition function relative to the density of receptor sites.
	Greek symbols
β_t	Mathematical function related to "F" function from Boyd model.
β	Parameter related to temperature and Boltzmann constant (1/J).
ε_1, ε_2, ΔE	Adsorption energy (J/mol).
μ	The chemical potential of the adsorbed molecule (J/mol).
μ_m	The chemical potential of the dissolved molecule (J/mol).
π	Constant.

Acknowledgments

The authors would like to thank the MESRS and DGRSDT (Ministère de l'Enseignement Supérieur et de la Recherche Scientifique et la Direction Générale de la Recherche Scientifique et du Développement Technologique- Algérie) for their Financial support.

9. References

[1] S.F. Azha, L. Sellaoui, M.S. Shamsudin, S. Ismail, A. Bonilla-Petriciolet, A. Ben Lamine, A. Erto, Synthesis and characterization of a novel amphoteric adsorbent coating for anionic and cationic dyes adsorption: Experimental investigation and statistical physics modelling, Chem. Eng. J. 351 (2018) 221–229. https://doi.org/10.1016/j.cej.2018.06.092.

[2] L. Sellaoui, T. Depci, A.R. Kul, S. Knani, A. Ben Lamine, A new statistical physics model to interpret the binary adsorption isotherms of lead and zinc on activated carbon, J. Mol. Liq. 214 (2016) 220–230. https://doi.org/10.1016/j.molliq.2015.12.080.

[3] L. Sellaoui, G.L. Dotto, S. Wjihi, J.O. Gonçalves, L.A.A. Pinto, A.B. Lamine, A. Erto, Thermodynamic analysis of single and binary adsorption of Food Yellow 4 and Food Blue 2 on CC-chitosan: Application of statistical physics and IAST models, J. Mol. Liq. 232 (2017) 499–505. https://doi.org/10.1016/j.molliq.2017.02.103.

[4] H. Liu, J. Zhang, M. Lu, L. Liang, H. Zhang, J. Wei, Biosynthesis based membrane filtration coupled with iron nanoparticles reduction process in removal of dyes, Chem. Eng. J. 387 (2020) 124202. https://doi.org/10.1016/j.cej.2020.124202.

[5] A. Muniyasamy, G. Sivaporul, A. Gopinath, R. Lakshmanan, A. Altaee, A. Achary, P. Velayudhaperumal Chellam, Process development for the degradation of textile azo dyes (mono-, di-, poly-) by advanced oxidation process - Ozonation: Experimental & partial derivative modelling approach, J. Environ. Manage. 265 (2020) 110397. https://doi.org/10.1016/j.jenvman.2020.110397.

[6] H. Demissie, G. An, R. Jiao, T. Ritigala, S. Lu, D. Wang, Modification of high content nanocluster-based coagulation for rapid removal of dye from water and the mechanism, Sep. Purif. Technol. 259 (2021) 117845. https://doi.org/10.1016/j.seppur.2020.117845.

[7] A. Khatri, P.S. Rana, Visible light assisted photocatalysis of Methylene Blue and Rose Bengal dyes by iron doped NiO nanoparticles prepared via chemical co-precipitation, Phys. B Condens. Matter 579 (2020) 411905. https://doi.org/10.1016/j.physb.2019.411905.

[8] S. Li, Z. Zeng, W. Xue, Adsorption of lead ion from aqueous solution by modified walnut shell: kinetics and thermodynamics, Environ. Technol. 40 (2019) 1810–1820. https://doi.org/10.1080/09593330.2018.1430172.

[9] A. Mohammadi, A.H. Doctorsafaei, K.M. Zia, Alginate/calix[4]arenes modified graphene oxide nanocomposite beads: Preparation, characterization, and dye adsorption studies, Int. J. Biol. Macromol. 120 (2018) 1353–1361. https://doi.org/10.1016/j.ijbiomac.2018.09.136.

[10] N. Bouchelkia, H. Tahraoui, A. Amrane, H. Belkacemi, J.C. Bollinger, A. Bouzaza, A. Zoukel, J. Zhang, L. Mouni, Jujube stones based highly efficient activated carbon for methylene blue adsorption: kinetics and isotherms modeling, thermodynamics and mechanism study, optimization via Response surface methodology and machine learning approaches, Process Saf. Environ. Prot. (2022).

[11] H. Tahraoui, A.E. Belhadj, Z. Triki, N.R. Boudella, S. Seder, A. Amrane, J. Zhang, N. Moula, A. Tifoura, R. Ferhat, A. Bousselma, N. Mihoubi, Mixed Coagulant-flocculant Optimization for Pharmaceutical Effluent Pretreatment Using Response Surface Methodology and Gaussian Process Regression, Process Saf. Environ. Prot. (2022) S0957582022010102. https://doi.org/10.1016/j.psep.2022.11.045.

[12] N. Marzban, A. Moheb, S. Filonenko, S.H. Hosseini, M.J. Nouri, J.A. Libra, G. Farru, Intelligent modeling and experimental study on methylene blue adsorption by sodium alginate-kaolin beads, Int. J. Biol. Macromol. 186 (2021) 79–91.

[13] H. Mazaheri, M. Ghaedi, M.A. Azqhandi, A. Asfaram, Application of machine/statistical learning, artificial intelligence and statistical experimental design for the modeling and optimization of methylene blue and Cd (II) removal from a binary aqueous solution by natural walnut carbon, Phys. Chem. Chem. Phys. 19 (2017) 11299–11317.

[14] J. Qi, Y. Hou, J. Hu, W. Ruan, Y. Xiang, X. Wei, Decontamination of methylene Blue from simulated wastewater by the mesoporous rGO/Fe/Co nanohybrids: Artificial intelligence modeling and optimization, Mater. Today Commun. 24 (2020) 100709.

[15] S.D.K. Seera, D. Kundu, P. Gami, P.K. Naik, T. Banerjee, Synthesis and characterization of xylan-gelatin cross-linked reusable hydrogel for the adsorption of methylene blue, Carbohydr. Polym. 256 (2021) 117520. https://doi.org/10.1016/j.carbpol.2020.117520.

[16] M.A. Farghali, M.M. Abo-Aly, T.A. Salaheldin, Modified mesoporous zeolite-A/reduced graphene oxide nanocomposite for dual removal of methylene blue and Pb2+ ions from

wastewater, Inorg. Chem. Commun. 126 (2021) 108487. https://doi.org/10.1016/j.inoche.2021.108487.

[17] S. Mallakpour, V. Behranvand, Methylene blue contaminated water sanitization with alginate/compact discs waste-derived activated carbon composite beads: Adsorption studies, Int. J. Biol. Macromol. 180 (2021) 28–35. https://doi.org/10.1016/j.ijbiomac.2021.03.044.

[18] H. Wang, Z. Li, S. Yahyaoui, H. Hanafy, M.K. Seliem, A. Bonilla-Petriciolet, G. Luiz Dotto, L. Sellaoui, Q. Li, Effective adsorption of dyes on an activated carbon prepared from carboxymethyl cellulose: Experiments, characterization and advanced modelling, Chem. Eng. J. (2020) 128116. https://doi.org/10.1016/j.cej.2020.128116.

[19] Y. Ji, F. Xu, W. Wei, H. Gao, K. Zhang, G. Zhang, Y. Xu, P. Zhang, Efficient and fast adsorption of methylene blue dye onto a nanosheet MFI zeolite, J. Solid State Chem. 295 (2021) 121917. https://doi.org/10.1016/j.jssc.2020.121917.

[20] Y. Dehmani, O.E. Khalki, H. Mezougane, S. Abouarnadasse, Comparative study on adsorption of cationic dyes and phenol by natural clays, Chem. Data Collect. 33 (2021) 100674. https://doi.org/10.1016/j.cdc.2021.100674.

[21] T. Shen, S. Mao, F. Ding, T. Han, M. Gao, Selective adsorption of cationic/anionic tritoluene dyes on functionalized amorphous silica: A mechanistic correlation between the precursor, modifier and adsorbate, Colloids Surf. Physicochem. Eng. Asp. 618 (2021) 126435. https://doi.org/10.1016/j.colsurfa.2021.126435.

[22] R. Bushra, S. Mohamad, Y. Alias, Y. Jin, M. Ahmad, Current approaches and methodologies to explore the perceptive adsorption mechanism of dyes on low-cost agricultural waste: A review, Microporous Mesoporous Mater. (2021) 111040. https://doi.org/10.1016/j.micromeso.2021.111040.

[23] Y. Dehmani, M. Mobarak, R. Oukhrib, A. Dehbi, A. Mohsine, T. Lamhasni, Y. Tahri, H. Ahlafi, S. Abouarnadasse, E.C. Lima, M. Badawi, Adsorption of phenol by a Moroccan clay/ Hematite composite: Experimental studies and statistical physical modeling, J. Mol. Liq. 386 (2023) 122508. https://doi.org/10.1016/j.molliq.2023.122508.

[24] M. Padmapriya, S.T. Ramesh, V.M. Biju, Synthesis of seawater based geopolymer: Characterization and adsorption capacity of methylene blue from wastewater, Mater. Today Proc. (2021). https://doi.org/10.1016/j.matpr.2021.03.030.

[25] E. Alver, A.Ü. Metin, F. Brouers, Methylene blue adsorption on magnetic alginate/rice husk bio-composite, Int. J. Biol. Macromol. 154 (2020) 104–113. https://doi.org/10.1016/j.ijbiomac.2020.02.330.

[26] A.Q. Selim, L. Sellaoui, M. Mobarak, Statistical physics modeling of phosphate adsorption onto chemically modified carbonaceous clay, J. Mol. Liq. 279 (2019) 94–107. https://doi.org/10.1016/j.molliq.2019.01.100.

[27] M. Ben Manaa, N. Bouaziz, B. Schmaltz, F. Tran Van, A. Ben Lamine, Study of the effect of variation in temperature and pH on the adsorption process of natural Gardenia yellow dye into TiO2 mesoporous for dye sensitized solar cells using the statistical physics formalism: Physicochemical and thermodynamic investigation, Microporous Mesoporous Mater. 270 (2018) 82–92. https://doi.org/10.1016/j.micromeso.2018.05.007.

[28] M. Mobarak, E.A. Mohamed, A.Q. Selim, L. Sellaoui, A.B. Lamine, A. Erto, A. Bonilla-Petriciolet, M.K. Seliem, Surfactant–modified serpentine for fluoride and Cr(VI) adsorption in single and binary systems: Experimental studies and theoretical modeling, Chem. Eng. J. 369 (2019) 333–343. https://doi.org/10.1016/j.cej.2019.03.086.

[29] A. Guediri, A. Bouguettoucha, D. Chebli, N. Chafai, A. Amrane, Molecular dynamic simulation and DFT computational studies on the adsorption performances of methylene blue in aqueous solutions by orange peel-modified phosphoric acid, J. Mol. Struct. (2019) 127290. https://doi.org/10.1016/j.molstruc.2019.127290.

[30] C. López-Iglesias, A.M. Casielles, A. Altay, R. Bettini, C. Alvarez-Lorenzo, C.A. García-González, From the printer to the lungs: Inkjet-printed aerogel particles for pulmonary delivery, Chem. Eng. J. 357 (2019) 559–566. https://doi.org/10.1016/j.cej.2018.09.159.

[31] S. Farch, M.M. Yahoum, S. Toumi, H. Tahraoui, S. Lefnaoui, M. Kebir, M. Zamouche, A. Amrane, J. Zhang, A. Hadadi, L. Mouni, Application of Walnut Shell Biowaste as an Inexpensive Adsorbent for Methylene Blue Dye: Isotherms, Kinetics, Thermodynamics, and Modeling, Separations 10 (2023) 60. https://doi.org/10.3390/separations10010060.

[32] A. Imessaoudene, S. Cheikh, A. Hadadi, N. Hamri, J.C. Bollinger, A. Amrane, H. Tahraoui, A. Manseri, L. Mouni, Adsorption Performance of Zeolite for the Removal of Congo Red Dye: Factorial Design Experiments, Kinetic, and Equilibrium Studies, Separations 10 (2023) 57. https://doi.org/10.3390/separations10010057.

[33] M. Kebir, H. Tahraoui, M. Chabani, M. Trari, N. Noureddine, A.A. Assadi, A. Amrane, N. Ben Hamadi, L. Khezami, Water Cleaning by a Continuous Fixed-Bed Column for Cr (VI) Eco-Adsorption with Green Adsorbent-Based Biomass: An Experimental Modeling Study, Processes 11 (2023) 363.

[34] K. Sukla Baidya, U. Kumar, Adsorption of brilliant green dye from aqueous solution onto chemically modified areca nut husk, South Afr. J. Chem. Eng. 35 (2021) 33–43. https://doi.org/10.1016/j.sajce.2020.11.001.

[35] E.D. Revellame, D.L. Fortela, W. Sharp, R. Hernandez, M.E. Zappi, Adsorption kinetic modeling using pseudo-first order and pseudo-second order rate laws: A review, Clean. Eng. Technol. 1 (2020) 100032. https://doi.org/10.1016/j.clet.2020.100032.

[36] B. Wang, B. Gao, Y. Wan, Comparative study of calcium alginate, ball-milled biochar, and their composites on aqueous methylene blue adsorption, Environ. Sci. Pollut. Res. 26 (2019) 11535–11541. https://doi.org/10.1007/s11356-018-1497-1.

[37] J.P. Simonin, On the comparison of pseudo-first order and pseudo-second order rate laws in the modeling of adsorption kinetics, Chem. Eng. J. 300 (2016) 254–263. https://doi.org/10.1016/j.cej.2016.04.079.

[38] N.A. Rashidi, A. Bokhari, S. Yusup, Evaluation of kinetics and mechanism properties of CO2 adsorption onto the palm kernel shell activated carbon, Environ. Sci. Pollut. Res. 28 (2021) 33967–33979. https://doi.org/10.1007/s11356-020-08823-z.

[39] A. Mandal, N. Bar, S.K. Das, Phenol removal from wastewater using low-cost natural bioadsorbent neem (Azadirachta indica) leaves: Adsorption study and MLR modeling, Sustain. Chem. Pharm. 17 (2020) 100308. https://doi.org/10.1016/j.scp.2020.100308.

[40] X. Yao, L. Ji, J. Guo, S. Ge, W. Lu, Y. Chen, L. Cai, Y. Wang, W. Song, An abundant porous biochar material derived from wakame (Undaria pinnatifida) with high adsorption performance for three organic dyes, Bioresour. Technol. 318 (2020) 124082. https://doi.org/10.1016/j.biortech.2020.124082.

[41] R. Chakraborty, R. Verma, A. Asthana, S.S. Vidya, A.K. Singh, Adsorption of hazardous chromium (VI) ions from aqueous solutions using modified sawdust: kinetics, isotherm and thermodynamic modelling, Int. J. Environ. Anal. Chem. 0 (2019) 1–18. https://doi.org/10.1080/03067319.2019.1673743.

[42] C. Djama, A. Bouguettoucha, D. Chebli, A. Amrane, H. Tahraoui, J. Zhang, L. Mouni, Experimental and Theoretical Study of Methylene Blue Adsorption on a New Raw Material, Cynara scolymus—A Statistical Physics Assessment, Sustainability 15 (2023) 10364. https://doi.org/10.3390/su151310364.

[43] H.M.F. Freundlich, Over the adsorption in solution, J Phys Chem 57 (1906) 1100–1107.

[44] I. Langmuir, THE ADSORPTION OF GASES ON PLANE SURFACES OF GLASS, MICA AND PLATINUM., J. Am. Chem. Soc. 40 (1918) 1361–1403. https://doi.org/10.1021/ja02242a004.

[45] A. Yazidi, L. Sellaoui, G.L. Dotto, A. Bonilla-Petriciolet, A.C. Fröhlich, A.B. Lamine, Monolayer and multilayer adsorption of pharmaceuticals on activated carbon: Application of advanced statistical physics models, J. Mol. Liq. 283 (2019) 276–286. https://doi.org/10.1016/j.molliq.2019.03.101.

[46] A.H. Almuqrin, S. Wjihi, F. Aouaini, A.B. Lamine, New insights on physico-chemical investigation of bisphosphonate adsorption isotherm into apatite substrate using statistical

physics treatment, J. Mol. Liq. 310 (2020) 113230. https://doi.org/10.1016/j.molliq.2020.113230.

[47] A.Q. Selim, L. Sellaoui, S.A. Ahmed, M. Mobarak, E.A. Mohamed, A.B. Lamine, A. Erto, A. Bonilla-Petriciolet, M.K. Seliem, Statistical physics-based analysis of the adsorption of Cu2+ and Zn2+ onto synthetic cancrinite in single-compound and binary systems, J. Environ. Chem. Eng. 7 (2019) 103217. https://doi.org/10.1016/j.jece.2019.103217.

[48] B. Mohamed, Z. Qingyu, G. D. Moggridge, B.L. Abdelmottaleb, New insight in adsorption of pyridine on the two modified adsorbents types MN200 and MN500 by means of grand canonical ensemble, J. Mol. Liq. 263 (2018) 413–421. https://doi.org/10.1016/j.molliq.2018.05.008.

[49] N. Bouaziz, O. Kouira, F. Aouaini, L. Bukhari, S. Knani, S. Znaidia, A.B. Lamine, Adsorption of antibiotics by bentonite-chitosan composite: Phenomenological modeling and physical investigation of the adsorption process, Int. J. Biol. Macromol. 242 (2023) 125156. https://doi.org/10.1016/j.ijbiomac.2023.125156.

[50] A. Gómez-Avilés, L. Sellaoui, M. Badawi, A. Bonilla-Petriciolet, J. Bedia, C. Belver, Simultaneous adsorption of acetaminophen, diclofenac and tetracycline by organo-sepiolite: Experiments and statistical physics modelling, Chem. Eng. J. 404 (2021) 126601. https://doi.org/10.1016/j.cej.2020.126601.

[51] S. Wjihi, F. Aouaini, A.H. Almuqrin, A.B. Lamine, Physicochemical assessment of prednisone adsorption on two molecular composites using statistical physics formalism in cosmetics, Arab. J. Chem. 13 (2020) 6876–6886. https://doi.org/10.1016/j.arabjc.2020.06.040.

[52] M.B. Yahia, S. Knani, L.B.H. Hsan, M.B. Yahia, H. Nasri, A. Ben Lamine, Statistical studies of adsorption isotherms of iron nitrate and iron chloride on a thin layer of porphyrin, J. Mol. Liq. 248 (2017) 235–245. https://doi.org/10.1016/j.molliq.2017.10.073.

[53] B.M. Marwa, S. Bruno, B. Mongi, F. Tran Van, B.L. Abdelmottaleb, Modeling of adsorption isotherms of dye N719 on titanium oxide using the grand canonical ensemble in statistical physics for dye sensitized solar cells, Sol. Energy 135 (2016) 177–187. https://doi.org/10.1016/j.solener.2016.05.015.

[54] C. Djama, D. Chebli, A. Bouguettoucha, I. Doudou, A. Amrane, Statistical physics modelling of azo dyes biosorption onto modified powder of Acorus calamus in batch reactor, Biomass Convers. Biorefinery (2021). https://doi.org/10.1007/s13399-020-01190-2.

[55] N. Rahman, I. Ahmad, Insights into the statistical physics modeling and fractal like kinetic approach for the adsorption of As(III) on coordination polymer gel based on zirconium(IV) and 2-thiobarbituric acid, J. Hazard. Mater. 457 (2023) 131783. https://doi.org/10.1016/j.jhazmat.2023.131783.

[56] F. Dhaouadi, L. Sellaoui, G.L. Dotto, A. Bonilla-Petriciolet, A. Erto, A.B. Lamine, Adsorption of methylene blue on comminuted raw avocado seeds: Interpretation of the effect of salts via physical monolayer model, J. Mol. Liq. 305 (2020) 112815. https://doi.org/10.1016/j.molliq.2020.112815.

[57] L. Zhang, L. Yang, J. Chen, X. Zhou, Adsorption of SO2 and NH3 onto copper/graphene nanosheets composites: Statistical physics interpretations, thermodynamic investigations, and site energy distribution analyses, Chem. Eng. J. 446 (2022) 137224. https://doi.org/10.1016/j.cej.2022.137224.

[58] O. Amrhar, L. El Gana, M. Mobarak, Calculation of adsorption isotherms by statistical physics models: a review, Environ. Chem. Lett. 19 (2021) 4519–4547. https://doi.org/10.1007/s10311-021-01279-8.

[59] A. Guediri, A. Bouguettoucha, D. Chebli, A. Amrane, The use of encapsulation as a proposed solution to avoid problems encountered with conventional materials in powder form: Application in methylene blue removal from aqueous solutions, J. Mol. Liq. 316 (2020) 113841. https://doi.org/10.1016/j.molliq.2020.113841.

[60] H. Drucker, C.J. Burges, L. Kaufman, A. Smola, V. Vapnik, Support vector regression machines, Adv. Neural Inf. Process. Syst. 9 (1996).

[61] H. Tahraoui, A.E. Belhadj, A. Amrane, E.H. Houssein, Predicting the concentration of sulfate using machine learning methods, Earth Sci. Inform. (2022) 1–22.
[62] A. Hadadi, A. Imessaoudene, J.C. Bollinger, A. Bouzaza, A. Amrane, H. Tahraoui, L. Mouni, Aleppo pine seeds (Pinus halepensis Mill.) as a promising novel green coagulant for the removal of Congo red dye: Optimization via machine learning algorithm, J. Environ. Manage. 331 (2023) 117286.
[63] H. Tahraoui, A.E. Belhadj, N. Moula, S. Bouranene, A. Amrane, Optimisation and Prediction of the Coagulant Dose for the Elimination of Organic Micropollutants Based on Turbidity, Kem. U Ind. (2021). https://doi.org/10.15255/KUI.2021.001.
[64] H. TAHRAOUI, A.E. Belhadj, Optimisation de l'élimination des micropolluants organiques, 2021.
[65] E.H. Houssein, M.R. Saad, F.A. Hashim, H. Shaban, M. Hassaballah, Lévy flight distribution: A new metaheuristic algorithm for solving engineering optimization problems, Eng. Appl. Artif. Intell. 94 (2020) 103731.
[66] H. Moussa, F. Dahmoune, M. Hentabli, H. Remini, L. Mouni, Optimization of ultrasound-assisted extraction of phenolic-saponin content from Carthamus caeruleus L. rhizome and predictive model based on support vector regression optimized by dragonfly algorithm, Chemom. Intell. Lab. Syst. 222 (2022) 104493.
[67] A. Azari, M.H. Mahmoudian, M.H. Niari, I. Eş, E. Dehganifard, A. Kiani, A. Javid, H. Azari, Y. Fakhri, A.M. Khaneghah, Rapid and efficient ultrasonic assisted adsorption of diethyl phthalate onto FeIIFe2IIIO4@ GO: ANN-GA and RSM-DF modeling, isotherm, kinetic and mechanism study, Microchem. J. 150 (2019) 104144.
[68] G.K. Khiam, R.R. Karri, N.M. Mubarak, M. Khalid, R. Walvekar, E.C. Abdullah, M.E. Rahman, Modelling and optimization for methylene blue adsorption using graphene oxide/chitosan composites via artificial neural network-particle swarm optimization, Mater. Today Chem. 24 (2022) 100946.
[69] M. Kebir, I. kahina Benramdhan, N. Noureddine, H. Tahraoui, B. Nadia, B. Houssine, A. Rachid, J. Zhang, A.A. ASSADI, L. Mouni, Sunlight Degradation and Mineralization of Food Dye Photoinduced by Homogenous Photo Fenton Fe (III) and Fe (II)/Complex: Surface Response Modeling, (2023).
[70] M. Kebir, I.K. Benramdhan, N. Nasrallah, H. Tahraoui, N. Bait, H. Benaissa, R. Ameraoui, J. Zhang, A.A. Assadi, L. Mouni, Surface response modeling of homogeneous photo Fenton Fe (III) and Fe (II) complex for sunlight degradation and mineralization of food dye, Catal. Commun. 183 (2023) 106780.
[71] M. Nedjhioui, N. Nasrallah, M. Kebir, H. Tahraoui, R. Bouallouche, A.A. Assadi, A. Amrane, B. Jaouadi, J. Zhang, L. Mouni, Designing an Efficient Surfactant–Polymer–Oil–Electrolyte System: A Multi-Objective Optimization Study, Processes 11 (2023) 1314.
[72] D.R. Lima, E.C. Lima, C.S. Umpierres, P.S. Thue, G.A. El-Chaghaby, R.S. da Silva, F.A. Pavan, S.L.P. Dias, C. Biron, Removal of amoxicillin from simulated hospital effluents by adsorption using activated carbons prepared from capsules of cashew of Para, Environ. Sci. Pollut. Res. 26 (2019) 16396–16408. https://doi.org/10.1007/s11356-019-04994-6.
[73] H. Tahraoui, S. Toumi, A.H. Hassein-Bey, A. Bousselma, A.N.E.H. Sid, A.E. Belhadj, Z. Triki, M. Kebir, A. Amrane, J. Zhang, Advancing Water Quality Research: K-Nearest Neighbor Coupled with the Improved Grey Wolf Optimizer Algorithm Model Unveils New Possibilities for Dry Residue Prediction, Water 15 (2023) 2631.
[74] H. Tahraoui, A. Amrane, A.E. Belhadj, J. Zhang, Modeling the organic matter of water using the decision tree coupled with bootstrap aggregated and least-squares boosting, Environ. Technol. Innov. 27 (2022) 102419. https://doi.org/10.1016/j.eti.2022.102419.
[75] H. Tahraoui, A.E. Belhadj, A. Hamitouche, M. Bouhedda, A. Amrane, Predicting the concentration of sulfate (SO42-) in drinking water using artificial neural networks: a case study: Médéa-Algeria, DESALINATION WATER Treat. 217 (2021). https://doi.org/10.5004/dwt.2021.26813.

[76] H. Tahraoui, A.E. Belhadj, A. Hamitouche, Prediction of the Bicarbonate Amount in Drinking Water in the Region of Médéa Using Artificial Neural Network ModellingPredviđanje količine bikarbonata u pitkoj vodi regije Médéa modeliranjem umjetnom neuronskom mrežom, Kem. U Ind. 69 (2020) 595–602. https://doi.org/10.15255/KUI.2020.002.

[77] M.M. Yahoum, S. Toumi, S. Hentabli, H. Tahraoui, S. Lefnaoui, A. Hadjsadok, A. Amrane, M. Kebir, N. Moula, A.A. Assadi, Experimental Analysis and Neural Network Modeling of the Rheological Behavior of Xanthan Gum and Its Derivatives, Materials 16 (2023) 2565.

[78] S. Mechati, M. Zamouche, H. Tahraoui, O. Filali, S. Mazouz, I.N.E. Bouledjemer, S. Toumi, Z. Triki, A. Amrane, M. Kebir, Modeling and Optimization of Hybrid Fenton and Ultrasound Process for Crystal Violet Degradation Using AI Techniques, Water 15 (2023) 4274.

[79] A. Bousselma, D. Abdessemed, H. Tahraoui, A. Amrane, Artificial intelligence and mathematical modelling of the drying kinetics of pre-treated whole apricots, Kem. U Ind. 70 (2021) 651–667.

[80] M. Zamouche, M. Chermat, Z. Kermiche, H. Tahraoui, M. Kebir, J.C. Bollinger, A. Amrane, L. Mouni, Predictive Model Based on K-Nearest Neighbor Coupled with the Gray Wolf Optimizer Algorithm (KNN_GWO) for Estimating the Amount of Phenol Adsorption on Powdered Activated Carbon, Water 15 (2023) 493.

[81] M. Zamouche, H. Tahraoui, Z. Laggoun, S. Mechati, R. Chemchmi, M.I. Kanjal, A. Amrane, A. Hadadi, L. Mouni, Optimization and Prediction of Stability of Emulsified Liquid Membrane (ELM): Artificial Neural Network, Processes 11 (2023) 364.

[82] L. Das, P. Das, A. Bhowal, C. Bhattachariee, Treatment of malachite green dye containing solution using bio-degradable Sodium alginate/NaOH treated activated sugarcane baggsse charcoal beads: Batch, optimization using response surface methodology and continuous fixed bed column study, J. Environ. Manage. 276 (2020) 111272. https://doi.org/10.1016/j.jenvman.2020.111272.

[83] B. Işık, V. Uğraşkan, Adsorption of methylene blue on sodium alginate–flax seed ash beads: Isotherm, kinetic and thermodynamic studies, Int. J. Biol. Macromol. (2020). https://doi.org/10.1016/j.ijbiomac.2020.11.070.

[84] I. Dalponte Dallabona, G.G. de Lima, B.I. Cestaro, I. de S. Tasso, T.S. Paiva, E.J.G. Laureanti, L.M. de M. Jorge, B.J.G. da Silva, C.V. Helm, A.L. Mathias, R.M.M. Jorge, Development of alginate beads with encapsulated jabuticaba peel and propolis extracts to achieve a new natural colorant antioxidant additive, Int. J. Biol. Macromol. 163 (2020) 1421–1432. https://doi.org/10.1016/j.ijbiomac.2020.07.256.

[85] M.A. Khan, S.M. Wabaidur, M.R. Siddiqui, A.A. Alqadami, A.H. Khan, Silico-manganese fumes waste encapsulated cryogenic alginate beads for aqueous environment de-colorization, J. Clean. Prod. 244 (2020) 118867. https://doi.org/10.1016/j.jclepro.2019.118867.

[86] A.Ü. Metin, D. Doğan, M. Can, Novel magnetic gel beads based on ionically crosslinked sodium alginate and polyanetholesulfonic acid: Synthesis and application for adsorption of cationic dyes, Mater. Chem. Phys. 256 (2020) 123659. https://doi.org/10.1016/j.matchemphys.2020.123659.

[87] C.P. Pinheiro, L.M.K. Moreira, S.S. Alves, T.R.S. Cadaval Jr, L.A.A. Pinto, Anthocyanins concentration by adsorption onto chitosan and alginate beads: Isotherms, kinetics and thermodynamics parameters, Int. J. Biol. Macromol. (2020). https://doi.org/10.1016/j.ijbiomac.2020.10.250.

[88] A. De Rossi, C.V.T. Rigueto, A. Dettmer, L.M. Colla, J.S. Piccin, Synthesis, characterization, and application of Saccharomyces cerevisiae/alginate composites beads for adsorption of heavy metals, J. Environ. Chem. Eng. 8 (2020) 104009. https://doi.org/10.1016/j.jece.2020.104009.

[89] R. Ahmad, R. Kumar, Synthesis and Properties of Cellulose Carbon Encapsulated ZnO for Dye Removal, J. Dispers. Sci. Technol. 32 (2011) 737–740. https://doi.org/10.1080/01932691.2010.480869.

[90] J. Kazemi, V. Javanbakht, Alginate beads impregnated with magnetic Chitosan@Zeolite nanocomposite for cationic methylene blue dye removal from aqueous solution, Int. J. Biol. Macromol. 154 (2020) 1426–1437. https://doi.org/10.1016/j.ijbiomac.2019.11.024.

[91] B. Zhang, S. Yu, Y. Zhu, Y. Shen, X. Gao, W. Shi, J. Hwa Tay, Adsorption mechanisms of crude oil onto polytetrafluoroethylene membrane: Kinetics and isotherm, and strategies for adsorption fouling control, Sep. Purif. Technol. 235 (2020) 116212. https://doi.org/10.1016/j.seppur.2019.116212.

[92] M.F. Oliveira, M.G.C. da Silva, M.G.A. Vieira, Equilibrium and kinetic studies of caffeine adsorption from aqueous solutions on thermally modified Verde-lodo bentonite, Appl. Clay Sci. 168 (2019) 366–373. https://doi.org/10.1016/j.clay.2018.12.011.

[93] Y.H. Magdy, H. Altaher, Kinetic analysis of the adsorption of dyes from high strength wastewater on cement kiln dust, J. Environ. Chem. Eng. 6 (2018) 834–841. https://doi.org/10.1016/j.jece.2018.01.009.

[94] R.A. Fideles, G.M.D. Ferreira, F.S. Teodoro, O.F.H. Adarme, L.H.M. da Silva, L.F. Gil, L.V.A. Gurgel, Trimellitated sugarcane bagasse: A versatile adsorbent for removal of cationic dyes from aqueous solution. Part I: Batch adsorption in a monocomponent system, J. Colloid Interface Sci. 515 (2018) 172–188. https://doi.org/10.1016/j.jcis.2018.01.025.

[95] A.A. Kamath, N.G. Nayak, R. Sagar, Coconut flower sheath derived activated charcoal as efficient and cost effective adsorbent for crystal violet dye removal, Inorg. Chem. Commun. 134 (2021) 109077. https://doi.org/10.1016/j.inoche.2021.109077.

[96] I. Othman, M. Abu Haija, P. Kannan, F. Banat, Adsorptive Removal of Methylene Blue from Water Using High-Performance Alginate-Based Beads, Water. Air. Soil Pollut. 231 (2020) 396. https://doi.org/10.1007/s11270-020-04751-3.

[97] L. Sellaoui, É.C. Lima, G.L. Dotto, S.L.P. Dias, A. Ben Lamine, Physicochemical modeling of reactive violet 5 dye adsorption on home-made cocoa shell and commercial activated carbons using the statistical physics theory, Results Phys. 7 (2017) 233–237. https://doi.org/10.1016/j.rinp.2016.12.014.

[98] G.L. Dotto, L.A.A. Pinto, M.A. Hachicha, S. Knani, New physicochemical interpretations for the adsorption of food dyes on chitosan films using statistical physics treatment, Food Chem. 171 (2015) 1–7. https://doi.org/10.1016/j.foodchem.2014.08.098.

[99] L. Sellaoui, G.L. Dotto, E.C. Peres, Y. Benguerba, É.C. Lima, A.B. Lamine, A. Erto, New insights into the adsorption of crystal violet dye on functionalized multi-walled carbon nanotubes: Experiments, statistical physics and COSMO–RS models application, J. Mol. Liq. 248 (2017) 890–897. https://doi.org/10.1016/j.molliq.2017.10.124.

[100] I. Ben Khemis, M. Bouzid, N. Mechi, A. Ben Lamine, Statistical physics modeling and interpretation of the adsorption of enantiomeric terpenes onto the human olfactory receptor OR1A1, Int. J. Biol. Macromol. 171 (2021) 428–434. https://doi.org/10.1016/j.ijbiomac.2020.12.209.

[101] M.K. Seliem, M. Mobarak, Cr(VI) uptake by a new adsorbent of CTAB–modified carbonized coal: Experimental and advanced statistical physics studies, J. Mol. Liq. 294 (2019) 111676. https://doi.org/10.1016/j.molliq.2019.111676.

[102] F. Dhaouadi, L. Sellaoui, M. Badawi, H.E. Reynel-Ávila, D.I. Mendoza-Castillo, J.E. Jaime-Leal, A. Bonilla-Petriciolet, A.B. Lamine, Statistical physics interpretation of the adsorption mechanism of Pb2+, Cd2+ and Ni2+ on chicken feathers, J. Mol. Liq. 319 (2020) 114168. https://doi.org/10.1016/j.molliq.2020.114168.

[103] M. Khalfaoui, A.E. Ghali, C. Aguir, Z. Mohamed, M.H.V. Baouab, A.B. Lamine, Study on adsorption of herbicide onto functionalized cellulose extracted from Juncus acutus L. plant: Experimental results and theoretical modeling, Ind. Crops Prod. 67 (2015) 169–178. https://doi.org/10.1016/j.indcrop.2015.01.032.

[104] N. Bouaziz, M. Ben Manaa, A. Ben Lamine, Physicochemical and thermodynamic investigation of hydrogen absorption and desorption in LaNi3.8Al1.0Mn0.2 using the statistical physics modeling, Results Phys. 9 (2018) 1323–1334. https://doi.org/10.1016/j.rinp.2018.04.035.

[105] A.Q. Selim, E.A. Mohamed, M.K. Seliem, Deep insights into the organic carbon role in selectivity and adsorption mechanism of phosphate and crystal violet onto low–cost black limestone: Modelling and physicochemical parameters interpretation, Colloids Surf. Physicochem. Eng. Asp. 580 (2019) 123755. https://doi.org/10.1016/j.colsurfa.2019.123755.
[106] M. Ben Yahia, S. Knani, H. Dhaou, M.A. Hachicha, A. Jemni, A. Ben Lamine, Modeling and interpretations by the statistical physics formalism of hydrogen adsorption isotherm on LaNi4.75Fe0.25, Int. J. Hydrog. Energy 38 (2013) 11536–11542. https://doi.org/10.1016/j.ijhydene.2013.03.083.
[107] M. Mobarak, E.A. Mohamed, A.Q. Selim, F.M. Mohamed, L. Sellaoui, A. Bonilla-Petriciolet, M.K. Seliem, Statistical physics modeling and interpretation of methyl orange adsorption on high–order mesoporous composite of MCM–48 silica with treated rice husk, J. Mol. Liq. 285 (2019) 678–687. https://doi.org/10.1016/j.molliq.2019.04.116.
[108] L. Sellaoui, H. Guedidi, SarraWjihi, L. Reinert, S. Knani, L. Duclaux, A.B. Lamine, Experimental and theoretical studies of adsorption of ibuprofen on raw and two chemically modified activated carbons: new physicochemical interpretations, RSC Adv. 6 (2016) 12363–12373. https://doi.org/10.1039/C5RA22302D.
[109] L. Sellaoui, S. Knani, A. Erto, M.A. Hachicha, A. Ben Lamine, Equilibrium isotherm simulation of tetrachlorethylene on activated carbon using the double layer model with two energies: Steric and energetic interpretations, Fluid Phase Equilibria 408 (2016) 259–264. https://doi.org/10.1016/j.fluid.2015.09.022.
[110] R. Sivakumar, N.Y. Lee, Adsorptive removal of organic pollutant methylene blue using polysaccharide-based composite hydrogels, Chemosphere 286 (2022) 131890. https://doi.org/10.1016/j.chemosphere.2021.131890.
[111] V. Rocher, A. Bee, J.M. Siaugue, V. Cabuil, Dye removal from aqueous solution by magnetic alginate beads crosslinked with epichlorohydrin, J. Hazard. Mater. 178 (2010) 434–439. https://doi.org/10.1016/j.jhazmat.2010.01.100.
[112] T. Zhang, M. Li, L. Chen, H. Bai, W. Wang, Y. Zhao, Novel montmorillonite nanosheets-based hydrogel beads with high adsorption performance and structural strength for removal of dyes and heavy metals, Chem. Phys. Lett. 813 (2023) 140322. https://doi.org/10.1016/j.cplett.2023.140322.
[113] S. Soleimani, A. Heydari, M. Fattahi, A. Motamedisade, Calcium alginate hydrogels reinforced with cellulose nanocrystals for methylene blue adsorption: Synthesis, characterization, and modelling, Ind. Crops Prod. 192 (2023) 115999. https://doi.org/10.1016/j.indcrop.2022.115999.
[114] M. Kasbaji, M. Mennani, N. Grimi, M. Oubenali, M. Mbarki, H. EL Zakhem, A. Moubarik, Adsorption of cationic and anionic dyes onto coffee grounds cellulose/sodium alginate double-network hydrogel beads: Isotherm analysis and recyclability performance, Int. J. Biol. Macromol. 239 (2023) 124288. https://doi.org/10.1016/j.ijbiomac.2023.124288.
[115] J. Kurczewska, Chitosan-montmorillonite hydrogel beads for effective dye adsorption, J. Water Process Eng. 48 (2022) 102928. https://doi.org/10.1016/j.jwpe.2022.102928.
[116] A. Kausar, S.U. Rehman, F. Khalid, A. Bonilla-Petriciolet, D.I. Mendoza-Castillo, H.N. Bhatti, S.M. Ibrahim, M. Iqbal, Cellulose, clay and sodium alginate composites for the removal of methylene blue dye: Experimental and DFT studies, Int. J. Biol. Macromol. 209 (2022) 576–585. https://doi.org/10.1016/j.ijbiomac.2022.04.044.

Supporting Information

MB adsorption on the prepared beads is analyzed by the pseudo first order (PFO) pseudo second order (PSO) pseudo nth order (PNO), Intraparticle, and Boyd models, which are given by Eq. S1 to Eq. S5 (a. b) respectively.

Pseudo first order (PFO) [35,36]:

$$Q_{ads} = Q_e(1 - e^{K_1 t}) \quad \ldots\ldots S1$$

Pseudo second order (PSO) [35,36]:

$$Q_{ads} = K_2 Q_e^2 t/(1 + K_2 Q_e\, t) \quad \ldots\ldots S2$$

Pseudo nth order [37] :

$$Q_{ads} = Q_e - \left[(n-1)K_n t + Q_e^{(1-n)}\right]^{1/(1-n)} \quad \ldots\ldots S3$$

Intraparticle diffusion [38] :

$$Q_{ads} = K_{id} t^{0.5} + I \quad \ldots\ldots S4$$

The intraparticle model produces a line with an intercept (I) that can provide information about the boundary layer thickness. Furthermore, Boyd's model is given according to the following equations [39] :

$$F = \frac{Q_{ads}}{Q_e} = 1 - \left(\frac{6}{\pi^2}\right)\sum_{n=1}^{\infty}\left(\frac{1}{n^2}\right)e^{(-n^2\beta_t)} \quad \ldots\ldots S5$$

If F > 0.85 then

$$\beta_t = -0.04977 - ln(1 - F) \quad \ldots\ldots a$$

If F < 0.85 then

$$\beta_t = \left[\sqrt{\pi} - \sqrt{\pi - \left(\frac{\pi^2 F}{3}\right)}\right]^2 \quad \ldots\ldots b$$

Eqs. S6 and S7 present the mathematical expressions for the Langmuir [44] and Freundlich [43] models, respectively.

$$\frac{Q_{ads}}{Q_m} = \frac{K_L C_e}{1 + K_L C_e} \quad \text{.....S6}$$

$$Q_{ads} = K_F C_e^{1/n_F} \quad \text{.....S7}$$

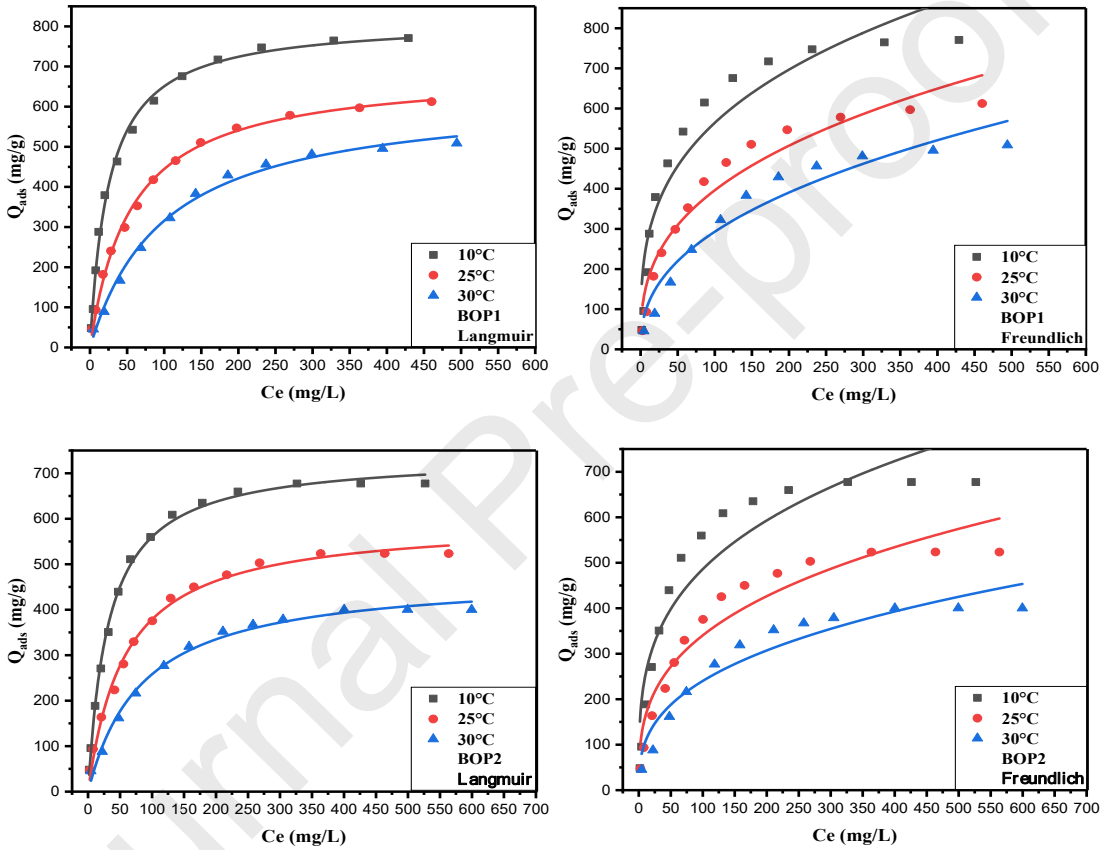

Figure S1. Langmuir and Freundlich modeling for MB adsorption isotherm onto BOP1 and BOP2 at various temperatures. (Agitation speed= 250 rpm, pH=6.2).